



# Fiducial Reference Measurements for Satellite Ocean Colour Phase-2

Complete characterisation and calibration results for  
FRMOCnet OCR models and re-characterisation  
routine: an update

FRM4SOC2-TR D7

Title	TR: Complete characterisation and calibration results for FRMOCnet OCR models and re-characterisation routine: an update
Document reference	FRM4SOC2- TR D7
Project	EUMETSAT – FRM4SOC Phase-2
Contract	EUMETSAT Contract No. EUM/CO/21/460002539/JIG
Deliverable	D-7
Version	3.1
Date issued	26.04.2023

Prepared By	Approved by
Name: Viktor Vabson	Name: Juan Ignacio Gossn
Organisation: UT	Organisation: EUMETSAT
Position: FRM4SOC Phase 2 Task 4 Leader	Position: FRM4SOC Phase 2 Project Officer
Date: 26.04.2023	Date:
Signature: 	Signature: 



	<b>EUMETSAT Contract no. EUM/CO/21/460002539/JIG Fiducial Reference Measurements for Satellite Ocean Colour (FRM4SOC Phase-2)</b>	Date: 26.04.2023 Page 1 (48) Ref: FRM4SOC2-TR-D7 Ver: 3.1
--	---	--

# Fiducial Reference Measurements for Satellite Ocean Colour Phase-2

*TR: Complete characterisation and calibration results  
for FRMOCnet OCR models and re-characterisation  
routine: an update (FRM4SOC2-TR D7)*

## TECHNICAL REPORT

Viktor Vabson, Ilmar Ansko, Riho Vendt, Joel Kuusk



UNIVERSITY OF TARTU  
Tartu Observatory

2023



PROGRAMME OF  
THE EUROPEAN UNION



IMPLEMENTED BY



	<b>EUMETSAT Contract no. EUM/CO/21/460002539/JIG Fiducial Reference Measurements for Satellite Ocean Colour (FRM4SOC Phase-2)</b>	Date: 26.04.2023 Page 2 (48) Ref: FRM4SOC2-TR-D7 Ver: 3.1
--	---	--

### Document Control Table

Title	TR: Complete characterisation and calibration results for FRMOCnet OCR models and re-characterisation routine: an update
Document reference	FRM4SOC2- TR D7
Project	EUMETSAT – FRM4SOC Phase-2
Contract	EUMETSAT Contract No. EUM/CO/21/460002539/JIG
Deliverable	D-7
Version	3.1
Date Issued	26.04.2023

### Document Change Record

Index	Issue	Revision	Date	Brief description	Issued by
1	1	0	08.04.2022	Original version	V. Vabson
2	2	0	11.07.2022	Updates after EUMETSAT review	V. Vabson
3	2	1	14.10.2022	Updates after ERB review	V. Vabson
4	2	2	03.11.2022	Updates after PM6	V. Vabson
5	3	0	06.02.2023	Updates after PM7	V. Vabson
6	3	1	26.04.2023	Release for publication	V. Vabson

### Distribution List

Public at <https://frm4soc2.eumetsat.int>



<b>EUMETSAT Contract no. EUM/CO/21/460002539/JIG</b> <b>Fiducial Reference Measurements for Satellite Ocean</b> <b>Colour (FRM4SOC Phase-2)</b>	Date: 26.04.2023 Page 3 (48) Ref: FRM4SOC2-TR-D7 Ver: 3.1
---	--

## Acronyms and Abbreviations

<b>Acronym</b>	<b>Description</b>
AAOT	Acqua Alta Oceanographic Tower
AERONET-OC	The Ocean Colour component of the Aerosol Robotic Network
AMT	Atlantic Meridional Transect
BRDF	Bidirectional reflectance distribution function
Cal	Calibration
CCPR	Consultative Committee for Photometry and Radiometry
CEOS	Committee on Earth Observation Satellites
Char	Characterization
CIPM	Comité International des Poids et Mesures (International Committee for Weights and Measures)
CIPM MRA	CIPM Mutual Recognition Arrangement
DR	Dynamic range
EO	Earth Observation
ESA	European Space Agency
EUMETSAT	European Organisation for the Exploitation of Meteorological Satellites
FICE	Fiducial Inter-Comparison Experiment
FOV	Field of view
FRM	Fiducial Reference Measurements
FRMOCnet	Copernicus FRM-certified OC instrument network
FRM4SOC	Fiducial Reference Measurements for Satellite Ocean Colour
FWHM	Full Width at Half Maximum
GEO	Group on Earth Observations
ILAC	International Laboratory Accreditation Cooperation
IOCCG	International Ocean-Colour Coordinating Group
IP module	Inclination-Pressure module
LUT	Look Up Table
MERIS	Medium Resolution Imaging Spectrometer
MMS1	Monolithic Miniature Spectrometer-1 of Zeiss with 256-channel NMOS array (Hamamatsu)
MVT	MERIS Validation Team
N/A	Not applicable
NASA	National Aeronautics and Space Administration
NERC	Natural Environment Research Council
NL	Noise level
NMI	National Metrology Institute
NPL	National Physical Laboratory
OC	Ocean Colour
OCDB	Ocean Colour Database
OCR	Ocean Colour Radiometer
PTFE	Polytetrafluoroethylene
QA	Quality Assurance
QA4EO	Quality Assurance framework for Earth Observation
QC	Quality Control
QTH	Quartz tungsten halogen
ROI	Return On Investment
RSP	Remote Sensing and Products Division
RD	Reference Document
S3	Sentinel-3
S3VT-OC	Sentinel-3 Validation Team – Ocean Colour group
SeaWiFS	Sea-Viewing Wide Field-of-View Sensor
SIRREX	SeaWiFS Intercalibration Round Robin Experiments
SI	International System of Units
SOW	Statement of Work
SST	Sea Surface Temperature



	<b>EUMETSAT Contract no. EUM/CO/21/460002539/JIG</b> <b>Fiducial Reference Measurements for Satellite Ocean</b> <b>Colour (FRM4SOC Phase-2)</b>	Date: 26.04.2023 Page 4 (48) Ref: FRM4SOC2-TR-D7 Ver: 3.1
--	---	--

<b>Acronym</b>	<b>Description</b>
TO	Tartu Observatory, University of Tartu
TR	Technical Report
UT	University of Tartu
VAL	Validation
VIM	Vocabulaire International de Métrologie (International Vocabulary in Metrology)
VTT MIKES	National Metrology Institute of Finland, Centre for Metrology



	<p align="center"><b>EUMETSAT Contract no. EUM/CO/21/460002539/JIG</b>  <b>Fiducial Reference Measurements for Satellite Ocean</b>  <b>Colour (FRM4SOC Phase-2)</b></p>	<p>Date: 26.04.2023  Page 5 (48)  Ref: FRM4SOC2-TR-D7  Ver: 3.1</p>
--	---	---

## Contents

Document Control Table .....	2
Document Change Record .....	2
Distribution List .....	2
Acronyms and Abbreviations.....	3
Contents .....	5
Applicable documents .....	6
Reference documents .....	6
1 Scope .....	7
2 Compatibility.....	7
3 Introduction .....	8
4 Description of radiometers subject to calibration and characterisation .....	8
5 Description of calibration results .....	11
5.1 Calibration standards.....	11
5.2 Calibration coefficients of radiometers.....	11
5.3 Calibration history of RAMSES and HyperOCR sensors.....	12
6 Description of characterisation results.....	14
6.1 Intrinsic properties of OCR contributing to the ocean colour products overall uncertainty budget .....	14
6.2 Stray light matrix.....	14
6.3 Immersion factor (irradiance, radiance) .....	16
6.4 Angular response of irradiance sensors in air.....	16
6.5 Angular response (FOV) of radiance sensors in air .....	18
6.6 Non-linearity of response.....	18
6.6.1 Comparison with previous characterisations.....	21
6.6.2 Spread of non-linearity coefficients .....	22
6.7 Accuracy of integration times .....	23
6.8 Dark signal .....	25
6.9 Thermal response.....	27
6.9.1 Comparison with previous results .....	29
6.9.2 Determination of sensor's temperature using the dark signal .....	32
6.9.3 Effects from temperature change.....	33
6.10 Polarisation sensitivity .....	38
6.11 Temporal response .....	39
6.12 Accuracy of wavelength scale.....	39
6.13 Signal-to-noise ratio .....	41
6.14 Pressure effects.....	43
7 Gaps in characterisation results .....	44
8 Conclusions .....	45
9 References .....	47
10 Acknowledgement .....	47



	<b>EUMETSAT Contract no. EUM/CO/21/460002539/JIG Fiducial Reference Measurements for Satellite Ocean Colour (FRM4SOC Phase-2)</b>	Date: 26.04.2023 Page 6 (48) Ref: FRM4SOC2-TR-D7 Ver: 3.1
--	---	--

### Applicable documents

ID	Description
[AD-0]	Statement of Work for FRM4SOC phase2, EUM/RSP/SOW/19/1131157
[AD-1]	ESA's contract no 4000117454/16/I-SBo ( <a href="https://frm4soc.org">https://frm4soc.org</a> )
[AD-2]	D-70: Technical Report TR-2 "A Review of Commonly used Fiducial Reference Measurement (FRM) Ocean Colour Radiometers (OCR) used for Satellite OCR Validation" (available at <a href="https://frm4soc.org/index.php/documents/deliverables/">https://frm4soc.org/index.php/documents/deliverables/</a> )
[AD-3]	'Statement of Work for Database of Ocean Colour In Situ Fiducial Reference Measurement Collections for Calibration and Validation', EUM/OPSCOPER/SOW/17/956607.
[AD-4]	IOCCG Protocol Series (2019). "Protocols for Satellite Ocean Colour Data Validation: In Situ Optical Radiometry". Zibordi, G., Voss, K. J., Johnson, B. C. and Mueller, J. L. IOCCG Ocean Optics and Biogeochemistry Protocols for Satellite Ocean Colour Sensor Validation, Volume 3.0, IOCCG, Dartmouth, NS, Canada. (Available at <a href="https://ioccg.org/what-we-do/ioccg-publications/oceanoptics-protocols-satellite-ocean-colour-sensor-validation/">https://ioccg.org/what-we-do/ioccg-publications/oceanoptics-protocols-satellite-ocean-colour-sensor-validation/</a> )
[AD-5]	K. Ruddick et. al., "A Review of Protocols for Fiducial Reference Measurements of Water-Leaving Radiance for Validation of Satellite Remote-Sensing Data over Water", Remote Sens. 2019, 11(19), 2198; <a href="https://doi.org/10.3390/rs11192198">https://doi.org/10.3390/rs11192198</a>
[AD-6]	K. Ruddick et. al., "A Review of Protocols for Fiducial Reference Measurements of Downwelling Irradiance for the Validation of Satellite Remote Sensing Data over Water", Remote Sens. 2019, 11(15), 1742; <a href="https://doi.org/10.3390/rs11151742">https://doi.org/10.3390/rs11151742</a>
[AD-7]	International Network for Sensor Inter-comparison and Uncertainty assessment for Ocean Color Radiometry (INSITU-OCR), <a href="http://ioccg.org/wpcontent/uploads/2016/02/INSITU-OCR-white-paper.pdf">http://ioccg.org/wpcontent/uploads/2016/02/INSITU-OCR-white-paper.pdf</a> .
[AD-8]	D-80a: Technical Report TR-3a "Protocols and Procedures to Verify the Performance of Reference Irradiance Sources used by Fiducial Reference Measurement Ocean Colour Radiometers for Satellite Validation" (available at <a href="https://frm4soc.org/index.php/documents/deliverables/">https://frm4soc.org/index.php/documents/deliverables/</a> )
[AD-9]	D-80b Technical Report TR-3b "Protocols and Procedures to Verify the Performance of Reference Radiance Sources used by Fiducial Reference Measurement Ocean Colour Radiometers for Satellite Validation" (available at <a href="https://frm4soc.org/index.php/documents/deliverables/">https://frm4soc.org/index.php/documents/deliverables/</a> )
[AD-10]	Bialek, A.; Douglas, S.; Kuusk, J.; Ansko, I.; Vabson, V.; Vendt, R.; Casal, A.T. Example of Monte Carlo Method Uncertainty Evaluation for Above-Water Ocean Colour Radiometry. Remote Sens. 2020, 12, 780. <a href="https://doi.org/10.3390/rs12050780">https://doi.org/10.3390/rs12050780</a>
[AD-11]	TR-9 Technical Report "Results from the First FRM4SOC Field Inter-Comparison Experiment (FICE) of Ocean Colour Radiometers" (available at <a href="https://frm4soc.org/index.php/documents/deliverables/">https://frm4soc.org/index.php/documents/deliverables/</a> )
[AD-12]	IOCCG Ocean Optics & Biogeochemistry Protocols for Satellite Ocean Colour Sensor Validation ( <a href="https://ioccg.org/what-we-do/ioccg-publications/ocean-opticsprotocols-satellite-ocean-colour-sensor-validation/">https://ioccg.org/what-we-do/ioccg-publications/ocean-opticsprotocols-satellite-ocean-colour-sensor-validation/</a> )

### Reference documents

ID	Description
[RD-1]	ESA's contract no 4000117454/16/I-SBo ( <a href="https://frm4soc.org">https://frm4soc.org</a> )



	<p><b>EUMETSAT Contract no. EUM/CO/21/460002539/JIG</b>  <b>Fiducial Reference Measurements for Satellite Ocean Colour (FRM4SOC Phase-2)</b></p>	<p>Date: 26.04.2023  Page 7 (48)  Ref: FRM4SOC2-TR-D7  Ver: 3.1</p>
--	--	---

## 1 Scope

The current document is the deliverable D-7 of the FRM4SOC phase-2 project. The document collects updates of the complete characterisation and calibration results for FRMOCnet OCR selected models and characterisation routine as required by the terms of the Invitation To Tender (ITT) No. 20/220036 “Copernicus – Fiducial Reference Measurements for Satellite Ocean Colour (FRM4SOC phase-2) issued by EUMETSAT. The Strategy plan for the secondary laboratory cal/char inter-comparison exercise (D-11) and the definition and harmonisation of laboratory guidelines (D-12) were followed in the preparation of the document.

The main aim of the deliverable is to report the results of the full characterisation and calibration activities performed over a set of selected OCR instrument models, including identification and characterisation of uncertainty sources not fully covered in phase-1. In the document, results of repeated characterisations and calibrations for 20 TriOS RAMSES and 17 Sea-Bird Scientific HyperOCR sensors are presented. For some characterisations, several methods/procedures have been used and outcomes are analysed. Results from the targeted lab comparison exercise (D-13) are also taken into account.

From the analysis of repeated characterisations and calibrations results, a characterisation routine for FRMOCnet OCR selected models is proposed. After the discussion and review process and feedback from the Task 6 and 9, the second version of the document (D-7, v.2) will be delivered to EUMETSAT.

## 2 Compatibility

Table 2-1. Compatibility

No.	Requirement
1.	<p>SOW- Req. 28:  The Contractor shall identify remaining uncertainty sources and their full characterisation shall be carried out, for the OCR instrument models selected already in phase-1. The coordination and possible co-occurrence with the targeted lab intercomparison exercise of Task 6 shall be included. Outcome shall be delivered as a TR to EUMETSAT as v.1 to be available for discussion during OCR workshop (Task 8). After the discussion and review process and after feedback from Task 6 and 9, v.2 shall be delivered to EUMETSAT as the TR D-7.</p>





### 3 Introduction

Metrological traceability to the International System of Units [1] is the concept that links all metrological measurements to the SI through a series of calibrations or comparisons. Each step in this traceability chain has a rigorous documented uncertainty analysis. A number of round-robin experiments arranged during the last decades for testing and validation of performance, calibrations and characterisations of Ocean Colour Radiometer (OCR) instruments clearly demonstrated that firm traceability of measurements to the SI units must exist, and calibration at a National Metrology Institute (NMI) or at an accredited laboratory is the preferred option. The spectral responsivity of a radiometer is usually calibrated by measuring a known radiation source aligned at a specified distance. Procedures are well established and validated [2]–[7]. Unfortunately, specified and controlled conditions during the calibration in a laboratory may differ substantially from varying conditions, which may prevail during later use of the instrument. There can be significant differences between calibration and later field use regarding operating temperature, angular variation of the light field (especially for irradiance sensors), the intensity of the measured radiation, spectral variation of the target, etc. Each of these factors may interact with instrument individual properties when used in the field, and estimation of such uncertainties requires instrument characterisation in addition to the absolute radiometric calibration [8]–[10]. Characterisation results describe the properties of individual radiometers. However, the system of two to three radiometers is often used for the determination of remote-sensing reflectance and/or fully normalised water-leaving radiance. Data handling of the three-radiometer system, including uncertainty contributions, is substantially more complicated than the case of a single radiometer. Some parameters which contribute significantly in the case of a single radiometer may have almost no effect in a three radiometer system. For evaluating specific uncertainty contributions to the uncertainty of final products, a particular measurement model and a full set of relevant input quantities must be known. Besides calibration/characterization (cal/char) results, the model's input quantities include additional information, which must be acquired during field measurements. Therefore, the uncertainty contributions in final products due to specific parameters of radiometers cannot be specified in this document.

In total, 37 OCR-s were calibrated and characterised in FRM4SOC phase-2. However, 5 instruments failed during measurements and some cal/char results for these instruments are not available. The description of the calibrated and characterised instruments is given in Section 4. Calibration results are presented in Section 5. A full list of characterisations of FRM OCR instruments used to acquire field data for satellite ocean colour validation and doing above- and/or in-water measurements is presented in Section 6 as guided by the IOCGG protocols [8]. Gaps in cal/char results of FRM OCR are presented in section 7. Conclusions and lessons learned during recharacterisation in the frame of FRM4SOC Phase 2 are presented in section 8.

### 4 Description of radiometers subject to calibration and characterisation

The list of radiometers subject to the complete calibration and characterisation during the project is given in Table 4-1. The two most common OCR types (TriOS RAMSES and Sea-Bird Scientific HyperOCR) (both radiance L and irradiance E sensors) have been radiometrically calibrated, then characterised according to parameter's listed in Table 6-1, and then again recalibrated. Key parameters of the radiometers are in Table 4-2, *Figure 4-1*.

Table 4-1. List of radiometers characterised during FRM4SOC-2.

No.	Model	Serial No.	Type	Comments
1	RAMSES	SAM_8166	L	
2	RAMSES	SAM_8595	L	
3	RAMSES	<b>SAM_8329</b>	E	broken during characterisation and repaired in the factory, bi-stable responsivity
4	RAMSES	SAM_81A8	E	had issues, repaired in factory and IP module removed
5	RAMSES	<b>SAM_862D</b>	E	broken during characterisation, replaced by SAM_8697
6	RAMSES	SAM_862E	L	
7	RAMSES	SAM_8697	E	
8	RAMSES	SAM_8698	E	
9	RAMSES	SAM_8699	L	
10	RAMSES	SAM_874C	G2 L	
11	RAMSES	SAM_874E	G2 L	
12	RAMSES	SAM_874F	G2 E	
13	RAMSES	SAM_81D8	L	
14	RAMSES	SAM_81CA	E	
15	RAMSES	SAM_8268	L	

<b>EUMETSAT Contract no. EUM/CO/21/460002539/JIG</b> <b>Fiducial Reference Measurements for Satellite Ocean</b> <b>Colour (FRM4SOC Phase-2)</b>	Date: 26.04.2023 Page 9 (48) Ref: FRM4SOC2-TR-D7 Ver: 3.1
---	--

No.	Model	Serial No.	Type	Comments
16	RAMSES	<b>SAM_809F</b>	E	IP module not reported in factory files prevents automated pixel 32 correction
17	RAMSES	SAM_81C9	L	replacement SAM_80DA
18	RAMSES	<b>SAM_80DA</b>	L	Input optics window apparently in bad shape+responsivity decay. Replaced by SAM_81C9
19	HyperOCR	SAT0464	L	
20	HyperOCR	SAT2027	E	
21	HyperOCR	SAT2054	L	
22	HyperOCR	SAT0488	E	
23	HyperOCR	<b>SAT0385</b>	L	Possible wavelength scale issue
24	HyperOCR	SAT0386	L	
25	HyperOCR	SAT0206	L	
26	HyperOCR	SAT0233	E	
27	HyperOCR	SAT0234	E	
28	HypSTAR	120242	L, E	
29	RAMSES	SAM_81Bo	L	Lab comparison object
30	RAMSES	SAM_8598	E	Lab comparison object
31	HyperOCR	SAT2072	E	Lab comparison object
32	HyperOCR	SAT2073	L	Lab comparison object
33	HyperOCR	SAT0392	L	Spare for lab comparison
34	HyperOCR	SAT0496	E	Spare for lab comparison
35	HyperOCR	SAT0375	L	Not participating in AAOT
36	HyperOCR	SAT0376	L	Not participating in AAOT shutter broken, only cal, no char
37	HyperOCR	SAT0476	E	Not participating in AAOT

Table 4-2. Key parameters of the radiometers

Parameter	Unit	RAMSES		HyperOCR	
		irradiance	radiance	irradiance	radiance
Weight	kg	0.9		1.1	0.95
length*	mm	295	330	395	355
diameter	mm	48		60(70)	60
supply voltage	V	12**		9...18	
average power consumption	W	0.85		4	
temperature range	°C	+2...+40		-10...+50	
temperature control		without temperature stabilisation			
field of view	°	180	7	180	6
input aperture diameter	mm	7	15	21	20
Si photodiode array	-	CMOS logic compatible			
active area	-	pixel pitch: 25 µm; height: 2.5 mm			
wavelength range	nm	350...1000		305...900	
wavelength step	nm	3.3			
spectral bandwidth	nm	9.5			
pixel count	-	256			
integration time	ms	4...8192			
minimum sampling interval	s	1		0.25	
bits per sample	-	16			
responsivity @ 500 nm & 1 ms	µW <sup>-1</sup> m <sup>2</sup> nm	0.6	N/A	0.7	N/A
responsivity @ 500 nm & 1 ms	µW <sup>-1</sup> m <sup>2</sup> nmsr	N/A	0.1	N/A	0.02
internal shutter	-	no	no	yes	yes
internal temperature sensor	-	no	no	yes	yes

\*cable adds 70 mm

\*\*when using the provided cable



PROGRAMME OF  
THE EUROPEAN UNION



IMPLEMENTED BY





Figure 4-1. Example of radiometers characterised in the project: 1 - the case, 2 – Seabird’s HyperOCR radiance sensor, 3 - HyperOCR irradiance sensor, 4 - TriOS RAMSES radiance sensor, 5 - RAMSES irradiance sensor, 6 - HyperOCR connection harness, 7 - RAMSES connection harness, 8 - alignment jig, 9 - bubble level.

The radiometers contain a Zeiss MMS1 module spectrometer, proprietary front-end electronics and optical input elements in the watertight housing. The housing has cylindrical symmetry, with the optical input and signal connector in the opposite ends of the cylinder. The housing is fabricated from stainless steel (RAMSES) or Acetron (HyperOCR). The optical axis is expected to coincide with the centre of the cylinder. The wavelength scale and some other parameters are defined in the calibration files provided by the manufacturer.

## 5 Description of calibration results

### 5.1 Calibration standards.

Spectra of a 1 kW FEL lamp and a spectral radiance factor in a  $0^\circ:45^\circ$  geometry for a reflectance panel used for the radiometric calibration of hyperspectral radiometers are shown in *Figure 5-1*. For cal/char activities, three different FEL lamps and two reflectance panels have been used. The detailed descriptions of the calibration standards and set-ups are provided in D-12.

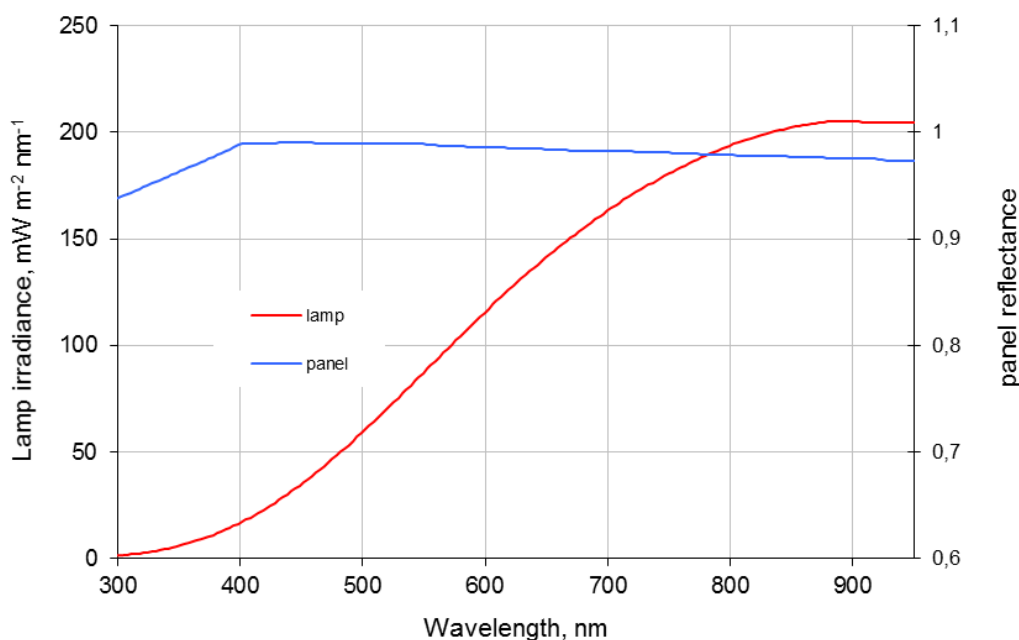


*Figure 5-1. Properties of the calibration standards used for calibration and characterisation of the OCR.*

### 5.2 Calibration coefficients of radiometers.

Calibration coefficients of two HyperOCR sensors and two RAMSES sensors are determined at  $21^\circ\text{C}$ . Raw signals and standard deviations of calibration measurements of RAMSES and HyperOCR sensors carried out for the determination of calibration coefficients are shown in

*Figure 5-2*. Signals of radiance sensors are on the left, and irradiance sensors are on the right side. Responsivity coefficients and standard uncertainty of RAMSES and HyperOCR sensors are given in *Figure 5-3*, with radiance sensors on the left and irradiance sensors on the right side. Radiometric calibration of the irradiance and radiance sensors and their uncertainty budgets are described in [11].

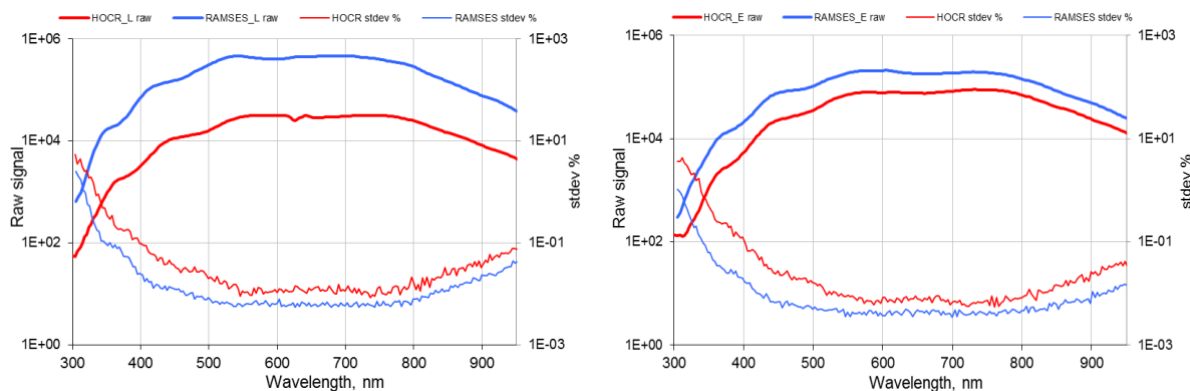


Figure 5-2. Raw signals and standard deviations of calibration measurements for the RAMSES and HyperOCR sensors. Left: radiance sensors SAM8595 and SAT0375; right: irradiance sensors SAM8329 and SAT0476.

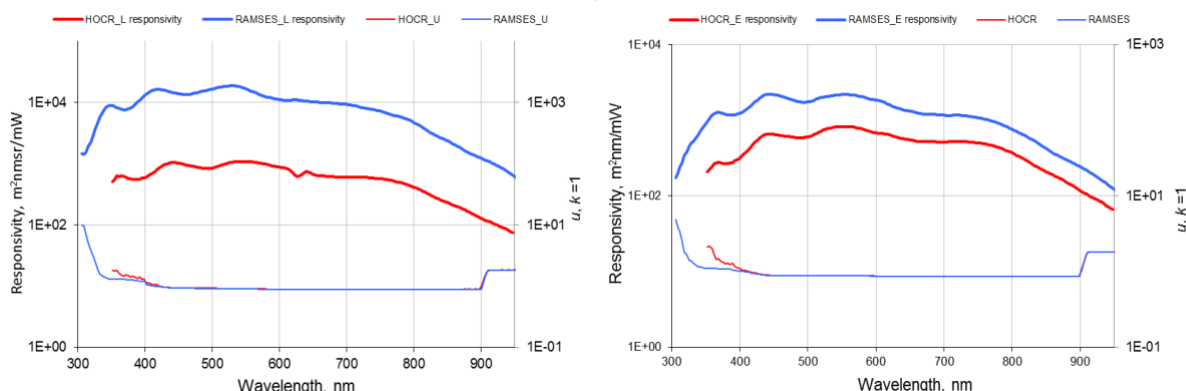


Figure 5-3. Responsivity coefficients and standard uncertainty of RAMSES and HyperOCR sensors. Left: radiance sensors SAM8595 and SAT0375; right: irradiance sensors SAM8329 and SAT0476.

### 5.3 Calibration history of RAMSES and HyperOCR sensors.

The calibration history of the hyperspectral radiometers calibrated at the optical laboratory of TO is available from 2016 to 2022. Different standard FEL lamps with traceability to different NMI-s (VTT MIKES, NPL, TU) have been used during this time period. The manufacturing date and type of sensors with calibration history are given in Table 5-1. The calibration history of the three RAMSES radiance sensors is presented in Figure 5-4, and the two RAMSES irradiance sensors in Figure 5-5. The calibration history of two HyperOCR sensors is provided during four year period in

Figure 5-6.

Table 5-1. Manufacturing date and type of sensors with calibration history.

Name	Type	Serial number	Manufacturing Date	Mean drift in year
RAMSES	irradiance	SAM 8329	2010	-0.8 %
RAMSES	irradiance	SAM 8598	2018	-2.3 %
RAMSES	radiance	SAM 8166	2004	-1.2 %
RAMSES	radiance	SAM 81B0	2006	-1.0 %
RAMSES	radiance	SAM 8595	2018	-1.1 %
HyperOCR	radiance	SAT 0222	2013	-1.6 %
HyperOCR	irradiance	SAT 0258	2013	-1.1 %

As seen from data in Table 5-1, on average, the drift of characterised radiometers is quite similar and close to -1 % per year.

**Thus, the requirement to recalibrate the radiometers at least once a year is well justified.**

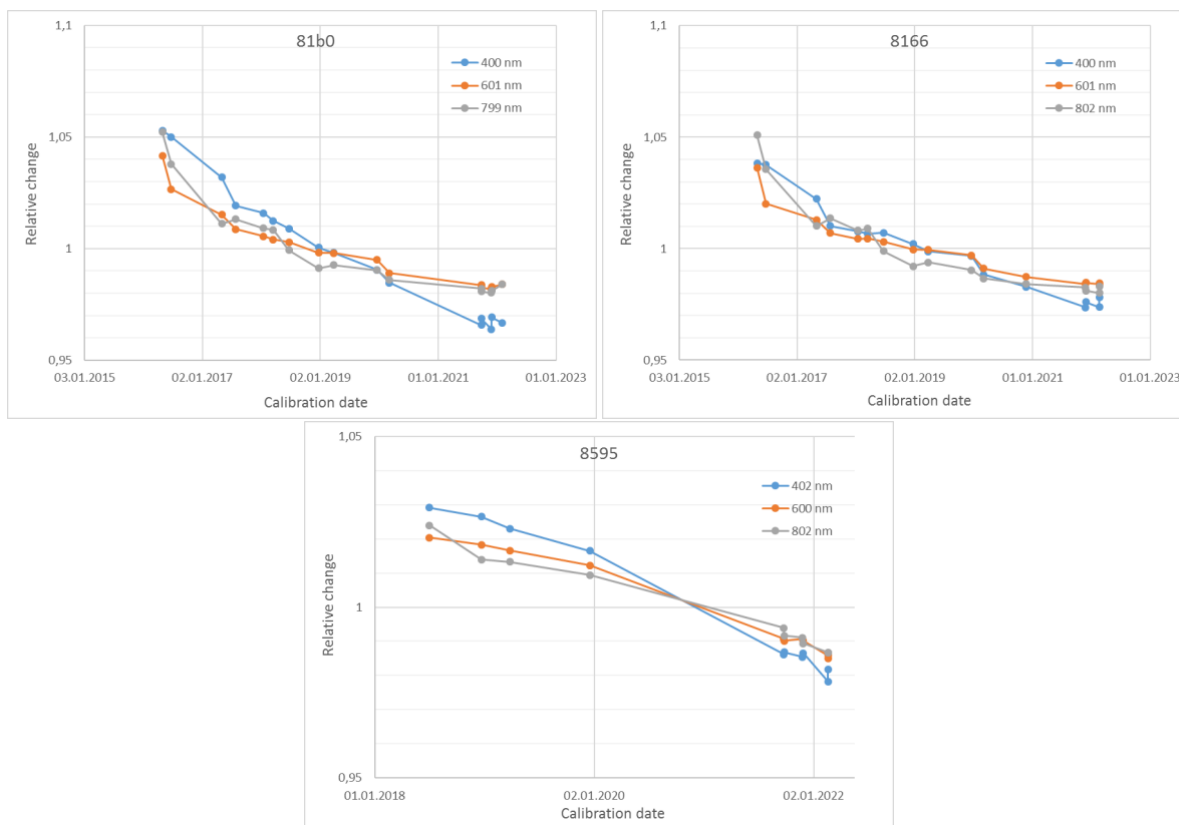


Figure 5-4. Calibration history of the RAMSES radiance sensors. The serial number of the sensor is indicated in the top of the chart.

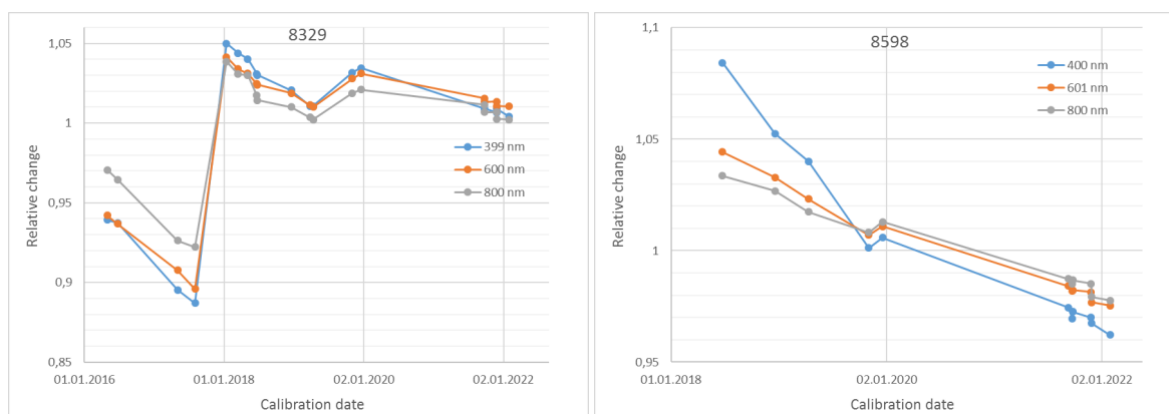


Figure 5-5. Calibration history of the RAMSES irradiance sensors. The serial number of the sensor is indicated in the top of the chart.

Responsivity jump in the left panel of Figure 5-5 occurred to RAMSES 8329 irradiance sensor in 2017 without any special maintenance between sequent calibrations. The radiometer has been involved in AMT27 exercise plus had transportation from Tartu lab there and back.



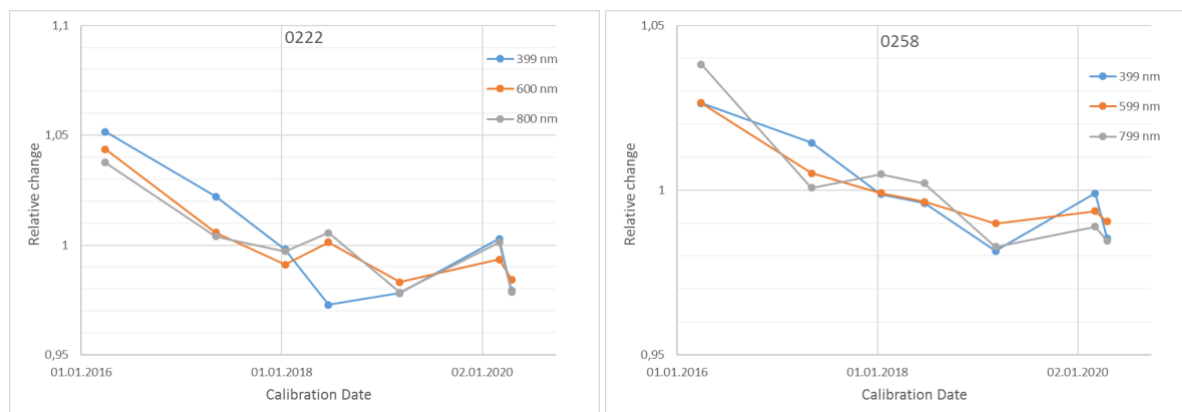


Figure 5-6. Calibration history of the HyperOCR radiance (left) and irradiance (right) sensors. The serial number of the sensor is indicated in the top of the chart.

## 6 Description of characterisation results

### 6.1 Intrinsic properties of OCR contributing to the ocean colour products overall uncertainty budget

The complete calibration and characterisation scheme for the two most common OCR types (TriOS RAMSES and Sea-Bird Scientific HyperOCR) was designed by following the guidelines of the IOCGG protocols [8] and the measurements performed in FRM4SOC Phase-1 [9], [10]. The structure of characterisation and calibration results of the hyperspectral OCR needed for the full description of uncertainty contributions which can affect field measurements is presented in Table 6-1.

Table 6-1. List of characterised OCR properties.

Parameter	Section
1. Absolute calibration for radiometric responsivity	5.2
2. Long term stability	5.3
3. Straylight and out of band response	6.2
4. Immersion factor (radiance, irradiance)	6.3
5. Angular response of irradiance sensors in air	6.4
6. Response angle (FOV) of radiance sensors in air	6.5
7. Non-linearity	6.6
8. Accuracy of integration times	6.7
9. Dark signal	6.8
10. Thermal sensitivity	6.9
11. Polarisation sensitivity	6.10
12. Temporal response	6.11
13. Wavelength scale	6.12
14. Signal-to-noise ratio	6.13
15. Pressure effects	6.14

### 6.2 Stray light matrix

The centre wavelength and bandpass of each band are required characterisations for any radiometer [8]. These are determined by the spectral response function, i.e., the passband, for each channel with a scanning monochromatic source exhibiting no stray light and a bandwidth tentatively less than 0.2 nm. Response functions are normalised to the maximum value to be equal to 1.0. In the proposed measurement procedure, for determination of the centre

wavelength the monochromator is iteratively tuned around the expected CWL until reaching the symmetric signal output (i.e. signal of the neighbouring pixels on both sides of the maximum do not differ by more than 20% from each other). In the case of the instrument classes of interest, this approach is equivalent to the centroid method, proposed in the [12].

In the case of a hyperspectral radiometer, the measurement process of determining the stray light matrix (SLM) consists of the following steps:

- 1) the initialisation of the hardware;
- 2) searching for the central wavelength for the given pixel of the spectroradiometer;
- 3) for each pixel, taking multiple readings from the spectroradiometer, including under- and overexposed samples;
- 4) saving the data files.

SLM consists of the set of bandpass functions – one for each pixel and describes a radiometer’s relative response at every pixel to a fixed monochromatic excitation at the central wavelength for the given pixel.

The examples of individual stray light matrices for RAMSES sensors is shown in *Figure 6-1*, and for HyperOCR sensor in *Figure 6-2*. All characterised instruments (both radiance and irradiance) show similar behaviour for the inband region, but out-of-band features are individual. Different radiometer types have different input optics, and different front-end electronics. Moreover, the MMS1 modules vary a lot. Generally, the stray light matrix for the irradiance sensor has the lower signal-to-noise ratio due to the instrument sensor sensitivity. The straylight matrix is an  $n \times n$  matrix where  $n$  is a number of pixels. Not all pixels are accessible for measurement. Parts of the matrix which cannot be determined experimentally are filled by hand in order to use matrix operators needed for calculations.

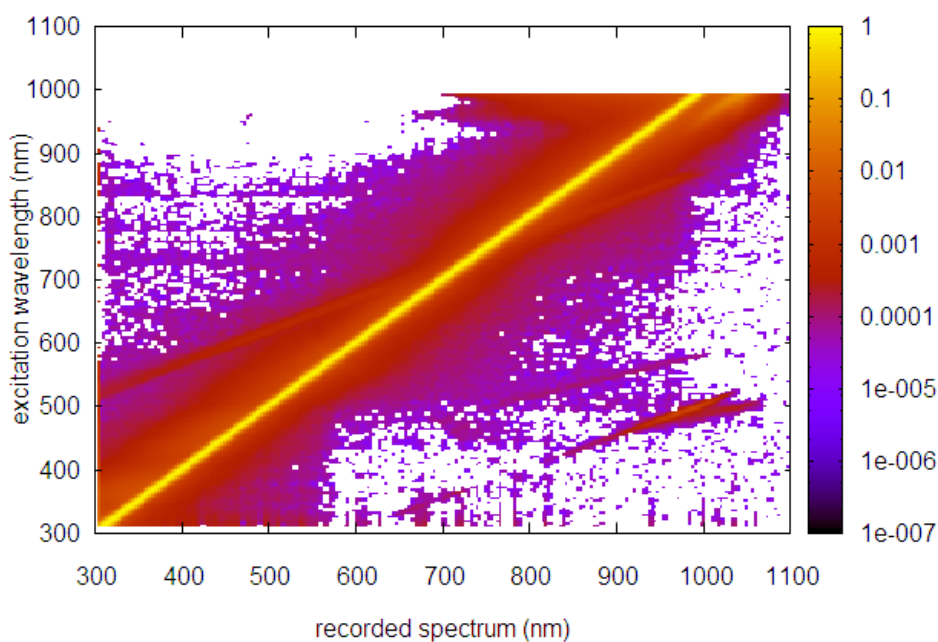


*Figure 6-1. Stray light matrix of a RAMSES radiance sensor (SAM8166). Diagonal values of the SLM are normalised to 1.*



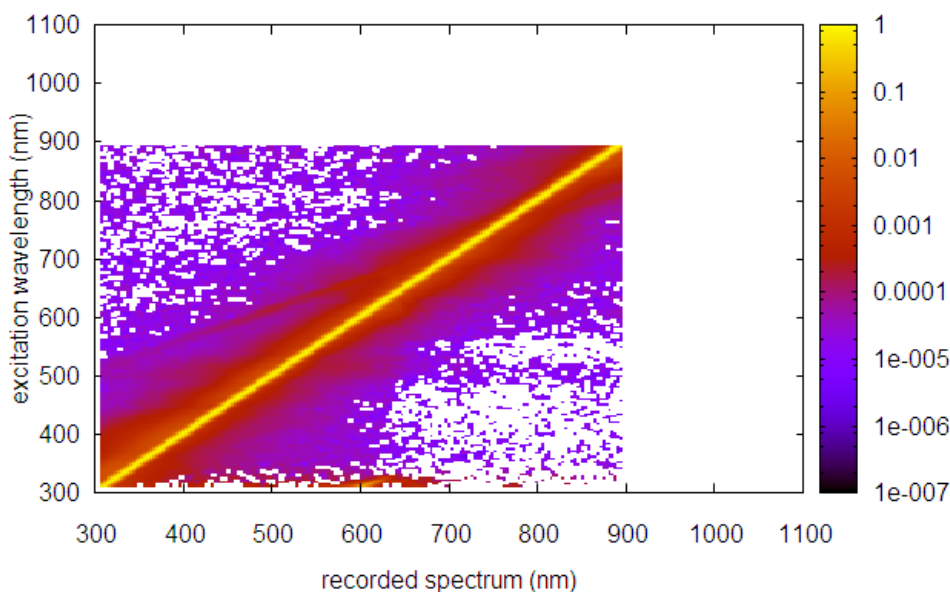


Figure 6-2. Stray light matrix of a HyperOCR radiance sensor (SAT2073). Diagonal values of the SLM are normalised to 1.

### 6.3 Immersion factor (irradiance, radiance)

Characterisation of the immersion factors of irradiance sensors at the JRC is planned for October 2022, where both types – the RAMSES and HyperOCR sensors, will be characterised. For characterisation, preliminary time and conditions have been agreed with Giuseppe Zibordi. JRC.

### 6.4 Angular response of irradiance sensors in air

The cosine response in the air of a HyperOCR irradiance sensor is shown in *Figure 6-3*. The results shown are rather common for HyperOCR sensors, i.e. a cosine response error usually within  $\pm 2\%$  in the range of incident angles from  $-60^\circ$  to  $+60^\circ$ .

The cosine response in the air of four RAMSES irradiance sensors is shown in *Figure 6-4*. Integral error of the two cosine collectors of *Figure 6-4* (upper half) together with the bars indicating limits of expanded uncertainty is shown in *Figure 6-5*. The cosine response error of RAMSES sensors is often significantly larger than the cosine response error of HyperOCR sensors, with much larger variability between individual sensors.

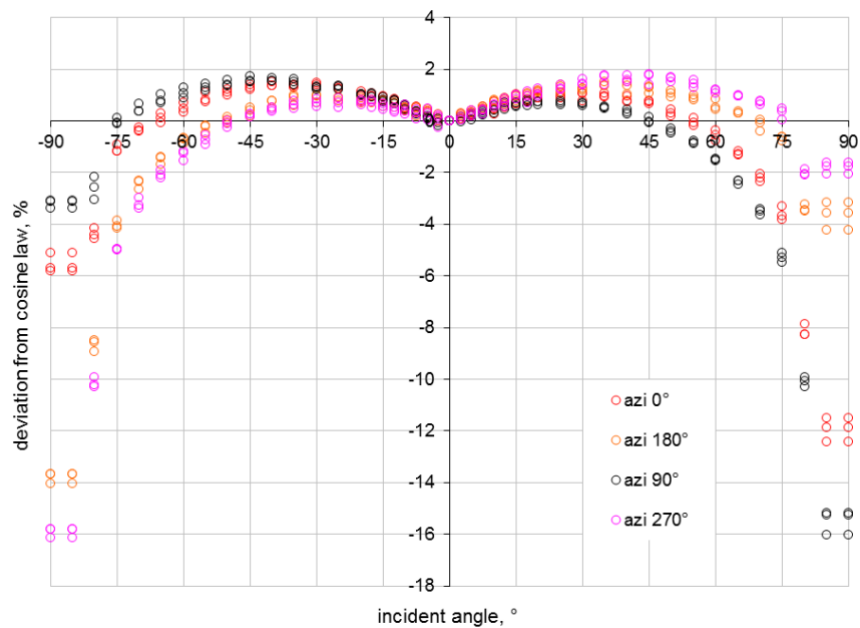


Figure 6-3. Angular response of a HyperOCR irradiance sensor (SAT2027).

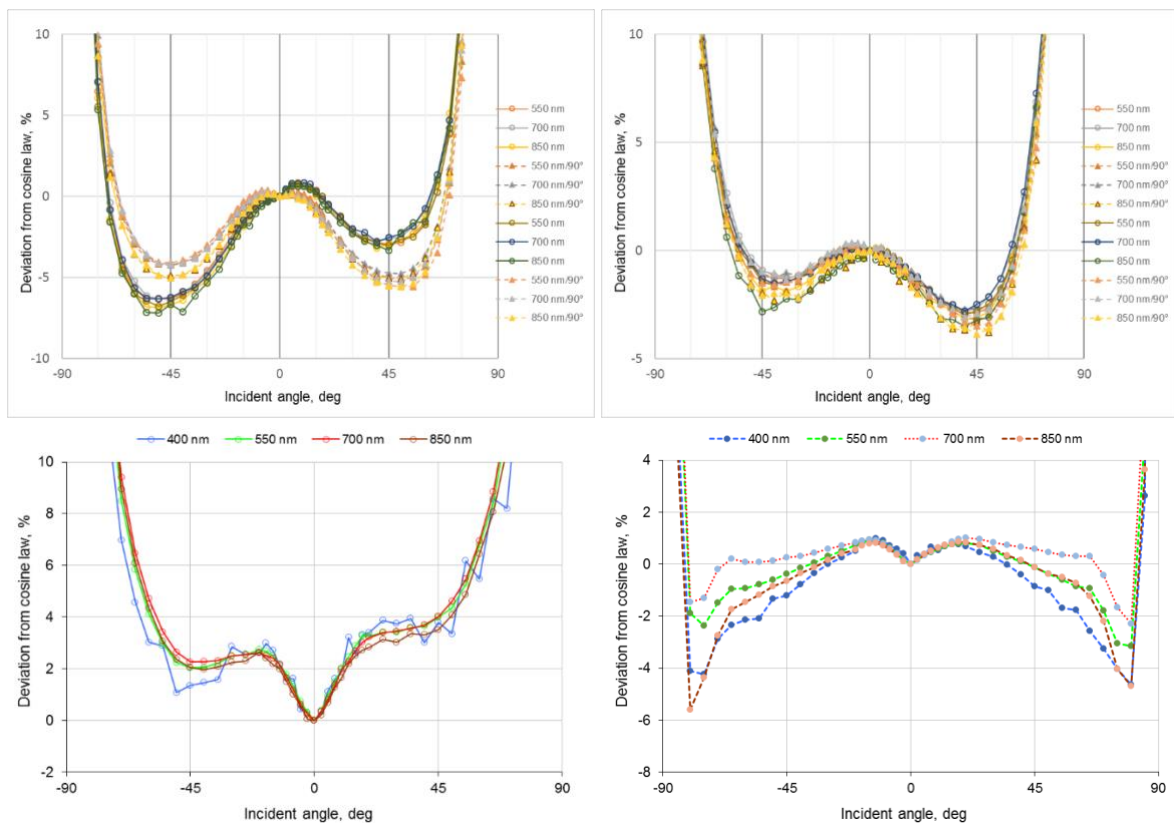


Figure 6-4. Angular response of four RAMSES irradiance sensors (83D4, 8301, 8329, 81A8).

As evident in Figure 6-4, angular response of RAMSES irradiance sensors is often asymmetrical. To guarantee reproducibility of characterisation results, for angular measurements of RAMSES irradiance sensors the sensor's azimuth angle shall be clearly defined and specified in the characterisation report.

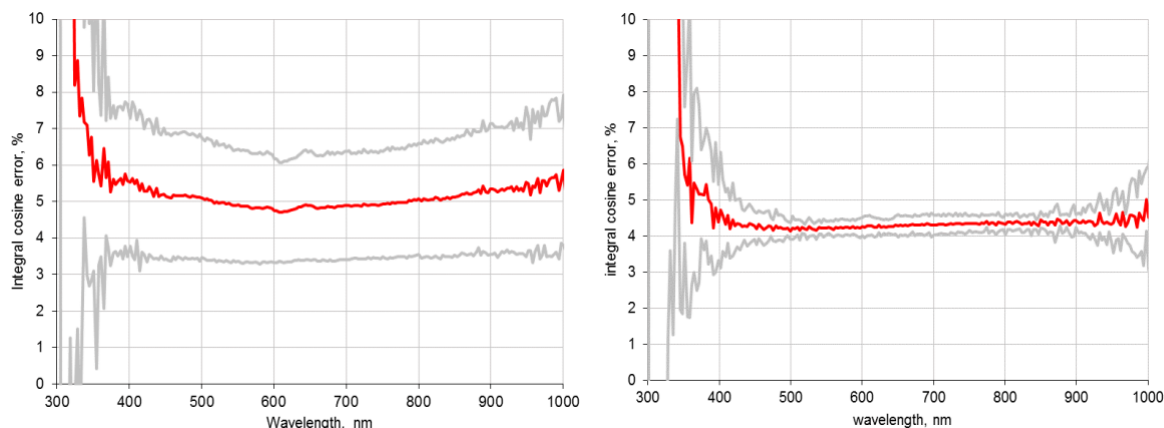


Figure 6-5. Integral cosine error with expanded uncertainty bars of two of the RAMSES irradiance sensors shown in Figure 6-4.

### 6.5 Angular response (FOV) of radiance sensors in air

The field of view (FOV) of the two HyperOCR radiance sensors is shown in Figure 6-6. Data presented in Figure 6-6 are suitable for determining the FOV at half maximum.

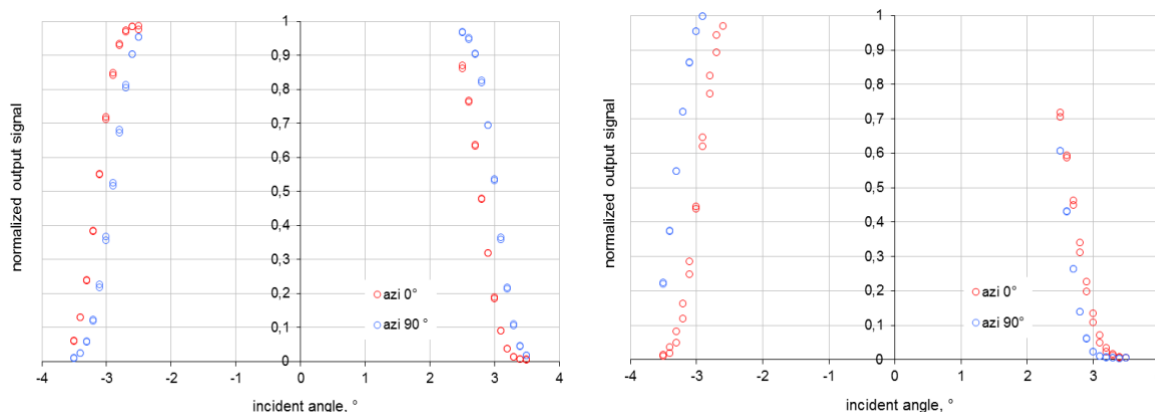


Figure 6-6. FOV of two above water HyperOCR radiance sensors (SAT0464 and SAT2054).

### 6.6 Non-linearity of response

For determination of the radiometric non-linearity, a stable light source (e.g. the calibration source) was measured by using at least two different integration times. Following [9], the absolute non-linearity error was determined, and from this, relative non-linearity error and coefficient  $\alpha$  were calculated. Non-linearity coefficient  $\alpha$  was measured at different temperatures, and for some sensors, moderate dependence of non-linearity on the temperature is evident. The size of the effect - deviation of coefficient  $\alpha(t_i)$  from the average value of  $\alpha$  - stays within  $\pm 10\%$ . The determination of relative non-linearity error and spectral non-linearity coefficient  $\alpha$  is described in D-12, see equations (9) to (13) in D12.

The non-linearity coefficient  $\alpha$  of the two HyperOCR radiance sensors measured at temperatures from 5 °C to 40 °C is shown in Figure 6-7. The relative non-linearity error of the same radiance sensors at the same temperatures is shown in Figure 6-8.

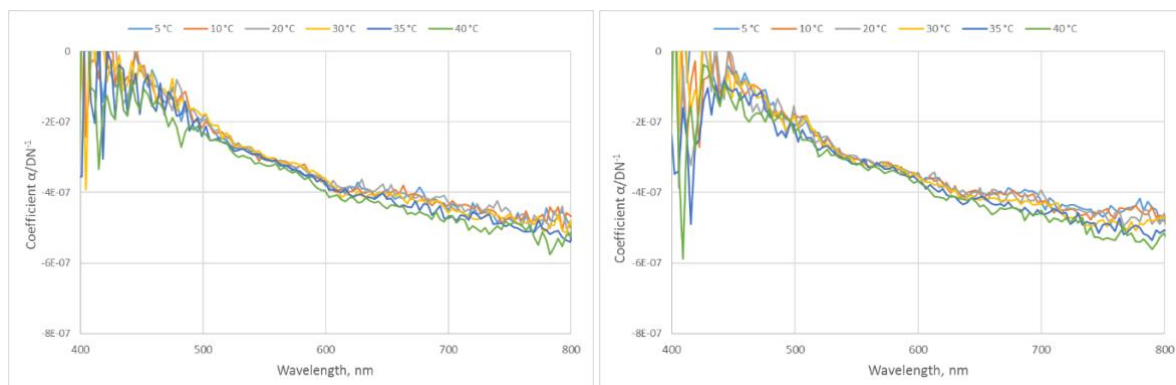


Figure 6-7. Spectral non-linearity coefficient  $\alpha$  of two HyperOCR radiance sensors (0375, 2054) as a function of temperature.

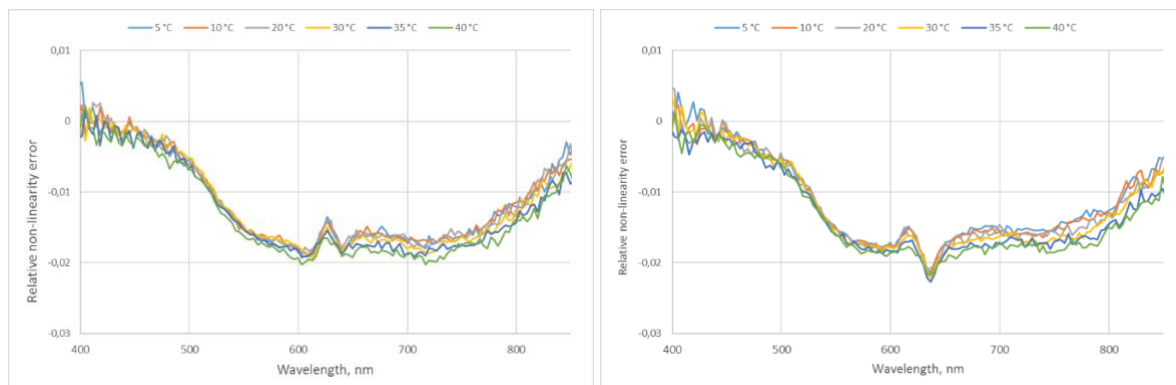


Figure 6-8. Relative non-linearity error of two HyperOCR radiance sensors (0375, 2054) as a function of wavelength and temperature.

The non-linearity coefficient  $\alpha$  of the two HyperOCR irradiance sensors measured at temperatures from 5 °C to 40 °C is shown in

Figure 6-9. The relative non-linearity error of the same irradiance sensors at the same temperatures is shown in Figure 6-10. In comparison with the radiance sensors (Figure 6-7, Figure 6-8), significantly stronger dependence on the ambient temperature is evident.

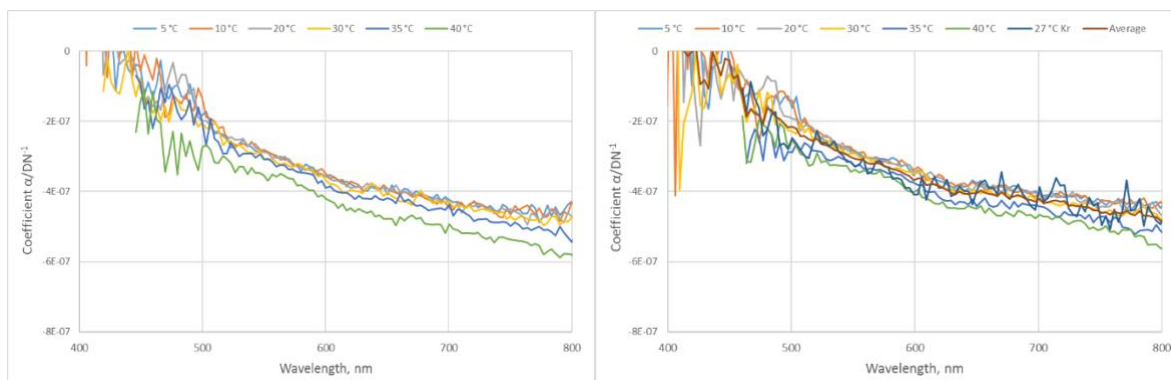


Figure 6-9. Spectral non-linearity coefficient  $\alpha$  of two HyperOCR irradiance sensors (0476, 2027) as a function of temperature.

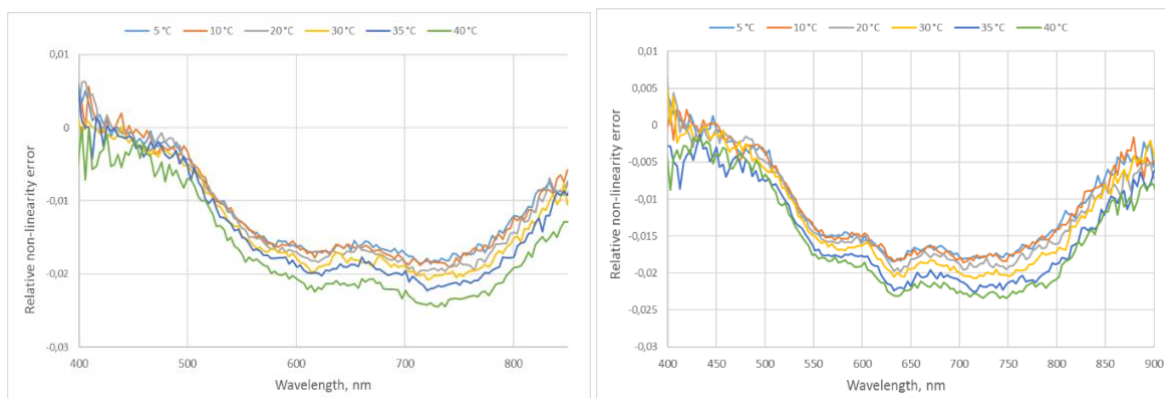


Figure 6-10. Relative non-linearity error of two HyperOCR irradiance sensors (0476, 2027) as a function of wavelength and temperature.

The non-linearity coefficient  $\alpha$  of the two RAMSES sensors measured at temperatures from 5 °C to 40 °C is shown in Figure 6-11, irradiance sensor left, and radiance sensor right. The relative non-linearity error of the same sensors at the same temperatures is shown in Figure 6-12. In the case of RAMSES sensors, dependence on the ambient temperature is less evident.

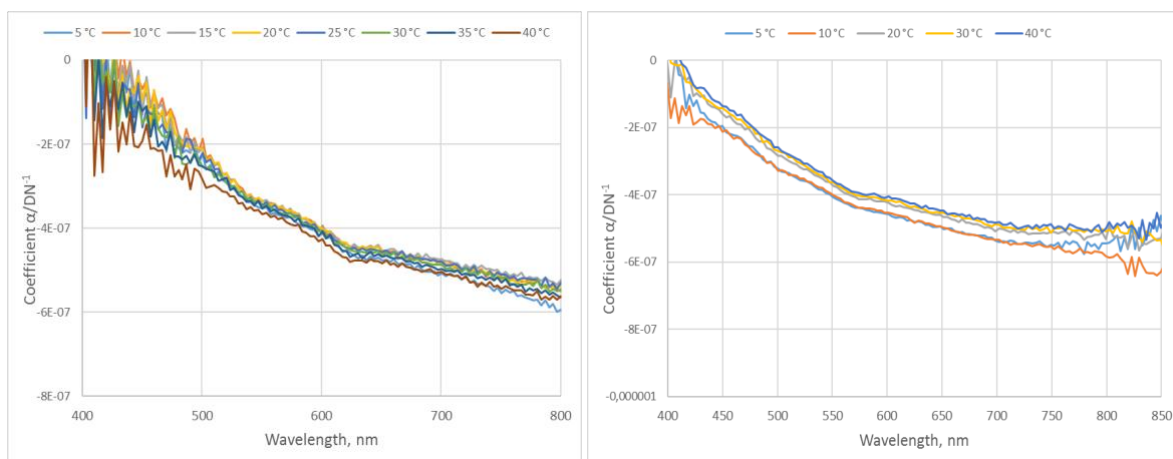


Figure 6-11. Spectral non-linearity coefficient  $\alpha$  of two RAMSES sensors as a function of temperature. Left (8598): irradiance; right (81Bo): radiance.

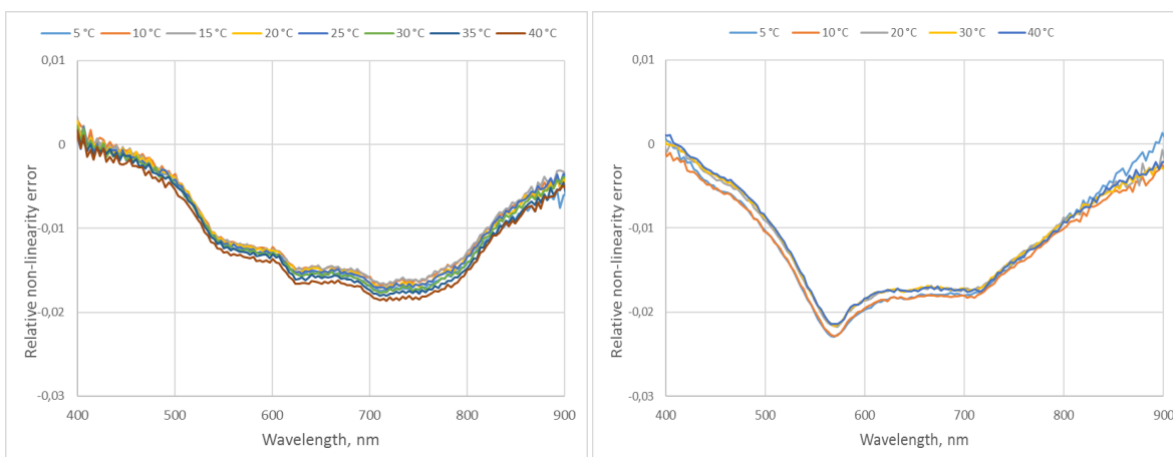


Figure 6-12. Relative non-linearity error of two RAMSES sensors as a function of wavelength and temperature. Left (8598): irradiance; right (8598): radiance.

### 6.6.1 Comparison with previous characterisations

The non-linearity coefficient  $\alpha(\lambda)$ , which does not depend upon the shape of the measured spectrum, is suitable characteristic for correcting both the laboratory and field results. Non-linearity coefficient  $\alpha(\lambda)$  in *Figure 6-13* and *Figure 6-14*, obtained by using the method based on two different integration times agrees reasonably well with the results of JRC, [13], based on a different method (using the inverse-square law describing the irradiance level created by the lamp as a function of the distance between the radiometer and the lamp at a fixed integration time setting). However, expanded uncertainty covering the non-linearity characteristics of [13] and [14] is not fully covering individual characteristics determined during FRM4SOC-2 project.

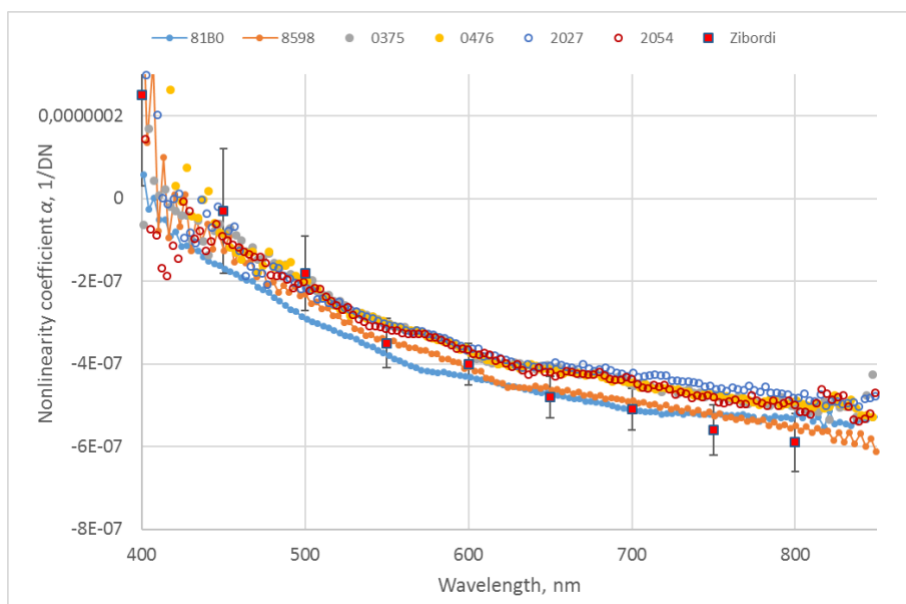


Figure 6-13. Non-linearity coefficient  $\alpha$  of two RAMSES and four HyperOCR radiometers. Results of JRC [13] and [14] are shown by red squares. Expanded uncertainty is covering the individual non-linearity characteristics determined in [13] and [14].

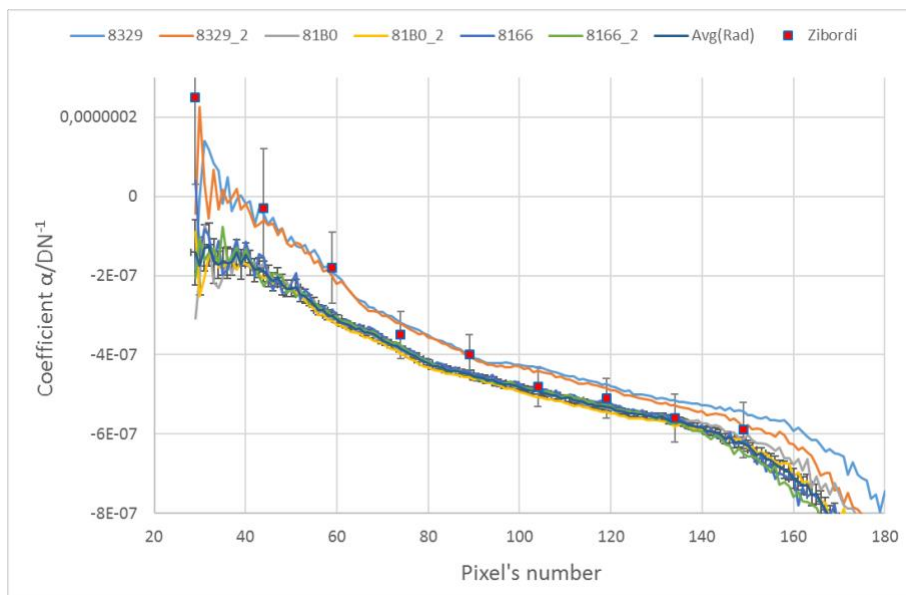
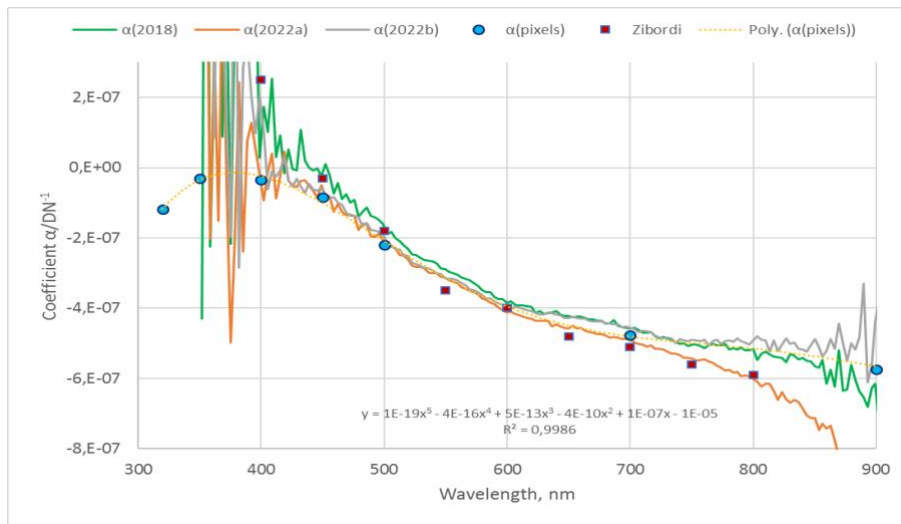


Figure 6-14. Non-linearity coefficients of RAMSES radiometers determined twice with 2-year space: two radiance (81B0; 8166) and an irradiance sensor (8329). Results of JRC in [13] and [14] for four RAMSES irradiance sensors are shown by red squares.



The method based on two different integration times can be modified by using a stable, adjustable monochromatic source set to the central wavelength of the certain (measured) pixel of the radiometer (*Figure 6-15*). Re-adjusting at each measured wavelength suitably the radiation intensity and the integration time of the radiometer, a more effective selection of signal level and, as a result, better signal-to-noise ratio in UV and NIR parts of the spectrum can be achieved. *Figure 5* shows the difference between non-linearity coefficients  $\alpha(\lambda)$  determined by using both methods. During radiometric calibration, the full-spectrum  $\alpha(\lambda)$  has been determined in 2018 and twice in 2022. Determination with an adjustable monochromatic source is made in 2022. In the central spectral part, the agreement between results is satisfactory. In the UV and NIR parts, determination by using the adjustable monochromatic source is clearly preferable and can be considered as validation/reference for the full-spectrum results.



*Figure 6-15. Non-linearity coefficient  $\alpha$  of RAMSES radiometer sensor (SAM 821E) determined during calibration (continuous lines) and by using adjustable monochromatic source (blue points). Results of JRC [13], [14] are shown by red squares.*

### 6.6.2 Spread of non-linearity coefficients

Spread of non-linearity coefficients for 16 RAMSES sensors is shown in *Figure 6-16* left and for 8 Hyper-OCR sensors in *Figure 6-16* right. Spread of RAMSES sensors is larger than of Hyper-OCR sensors, and significantly larger than uncertainty of an individual non-linearity characteristic.

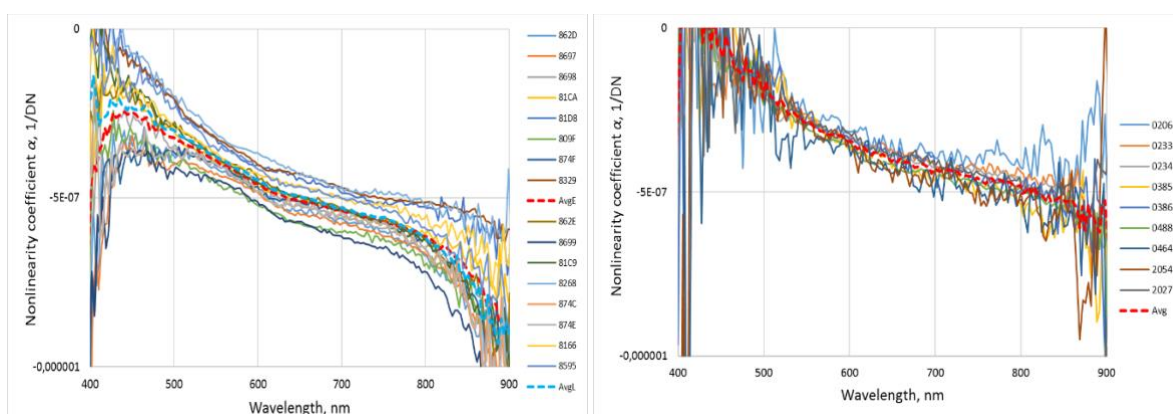


*Figure 6-16. Spread of non-linearity coefficients determined during FRM4SOC-2. RAMSES – left, HyperOCR – right.*

Class-specific presentation of non-linearity coefficients with expanded uncertainty basing on 16 RAMSES and 8 Hyper-OCR sensors is shown in *Figure 6-17*. The difference between RAMSES and HyperOCR sensors is evident, difference between irradiance and radiance sensors is insignificant.

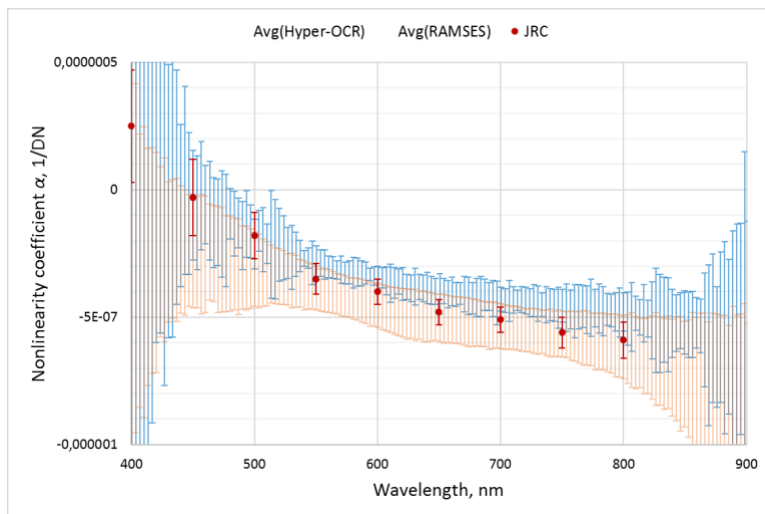


Figure 6-17. Class-specific presentation of non-linearity coefficients with expanded uncertainty. Results of the JRC [13], [14] are shown with red points.

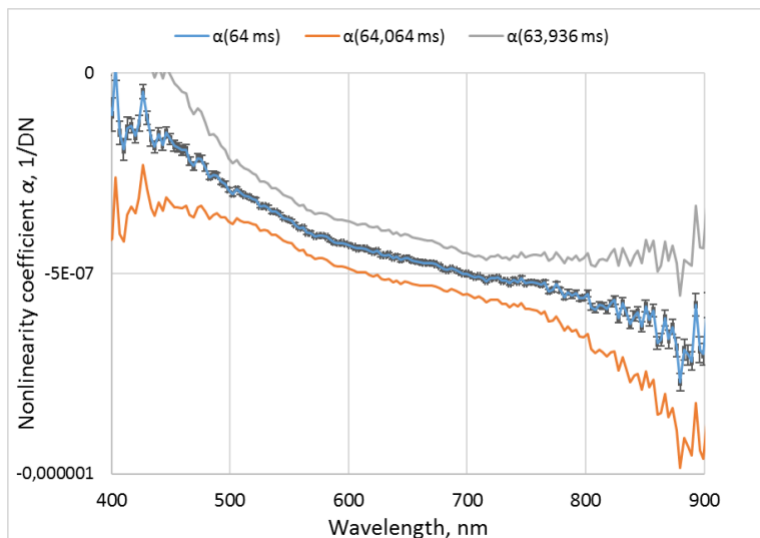


Figure 6-18. Sensitivity of non-linearity coefficient to small changes in integration time.

Influence of accuracy of the realized integration times on the possible spread of non-linearity coefficient is shown in Figure 6-18. Time with set value of 64 ms has been changed by ( $\pm 0.001$ ). This small deviation from the correct set value 64 ms will cause the changes in  $\alpha$  which are comparable with the spread of non-linearity coefficients shown in Figure 6-16 left for RAMSES sensors.

## 6.7 Accuracy of integration times

Measurements of non-linearity correction coefficients presented in this document are based solely on measurements of radiant exposure from a stable light source with different integration times. Radiant exposure is the radiant energy received by a surface per unit area or equivalently the irradiance of a surface, integrated over time of irradiation. In this measurement scheme, the non-linearity correction coefficient can be determined accurately only if integration times realised by a radiometer represent the set exposure time values correctly. The accuracy of realised integration times can be evaluated from the reproducibility of non-linearity results when three or more different integration times are used, leading to coincident or sufficiently close values. From all non-linearity results obtained for more than 40 radiometers, a clear deviation from the set values of the integration time was found in the case of the shortest (4 ms) integration time. An example for a HyperOCR radiance sensor is in Figure 6-19. The Xe-lamp spectra are measured by using four different integration times and normalised to the same radiant exposure. On the left panel, the spectrum measured with the set value of 4 ms is significantly deviating from the other three spectra (overlapping on the figure). After transforming the shortest integration time from the initial 4 ms to the expected actual value of 5 ms, good agreement is evident on the right panel of Figure 6-19. In the



case of the RAMSES instruments, the actual integration time is around 4.05 ms instead of 4 ms, as shown in figure 6-2. Applying such correction allows to get coherency with higher integration times.

The detected so far errors belong to the shortest integration time which is unlikely to be used during the field measurements. During the laboratory characterization measurements, wide range of integration times is used and the error might be significant, as shown in the *Figure 6-20*.

The detection method described here is indirect and only suitable to detect the outliers in respect of the 2:1 integration time ratio for the radiometers of interest. The absolute accuracy of the integration time needs different characterization scheme. Moreover, the absolute error will cancel out completely when the field and calibration measurements are conducted with the same integration times. So far, the integration time is auto-detected (i.e. arbitrary) during both the field and absolute calibration measurements and we strongly recommend to avoid the 4 ms integration time.

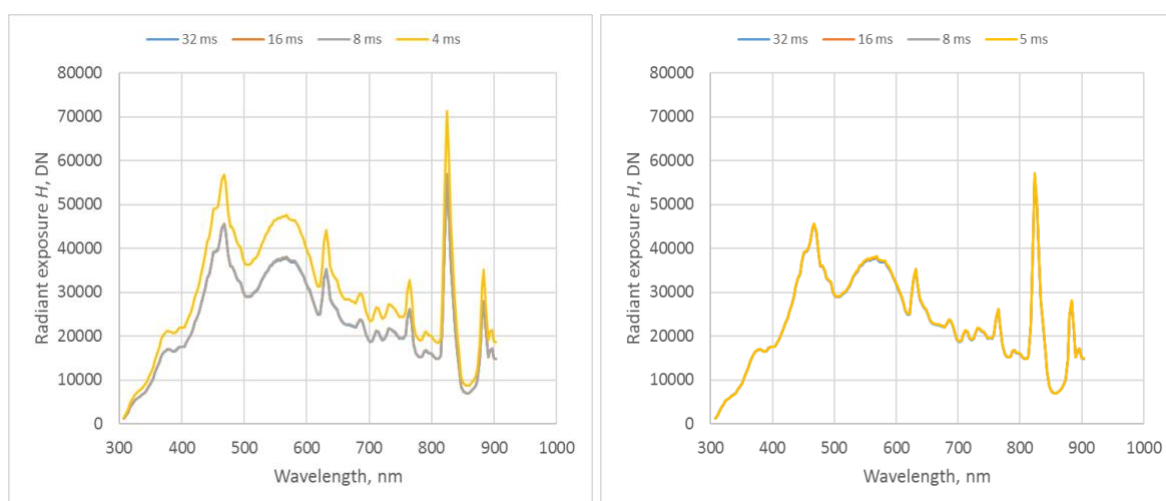


*Figure 6-19. Xe-lamp spectra measured by using four integration times and normalised to the same radiant exposure. Left: for set value 4 ms large bias is evident; right: after applying the actual value of 5 ms normal agreement is achieved.*

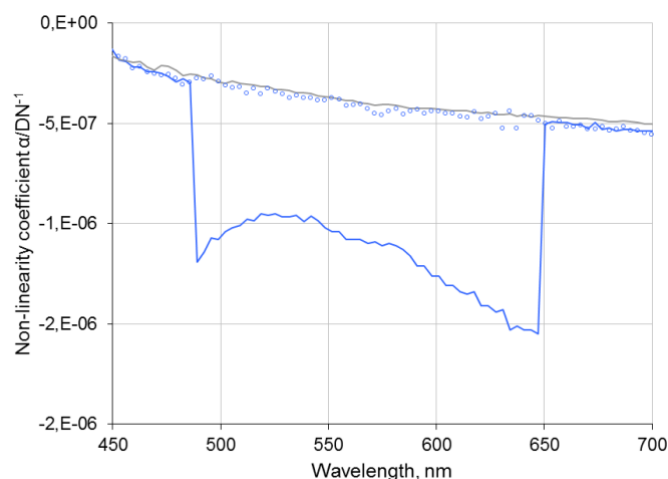


*Figure 6-20. Linearity coefficient alpha of the radiance sensor SAM\_8166. Gray line: from the radiometric calibration measurements, integration times of 32 and 64 ms; blue line: from monochromator measurements with variable integration times' blue circles: from monochromator measurements when using 4.05 ms instead of 4ms integration time.*

## 6.8 Dark signal

The output signal of the spectrometer is the sum of the target signal and the dark signal. The dark signal is the output signal when the optical entrance is closed. For the determination of the target signal, accurate knowledge of the dark signal is necessary. The dark signal of two RAMSES and two HyperOCR sensors were determined in the temperature range from 5 °C to 45 °C. The dependence of the dark signal as a function of integration time and temperature is given in *Figure 6-21*. As stated in the manual [15], the relation between dark signal and integration time shows a linear behaviour, and this is confirmed in *Figure 6-21* and *Figure 6-22*. However, the linear relationship is only valid at constant device temperature and has little practical value during the lab or field measurements under variable temperatures. Therefore, the recording of the dark signal in the field is indispensable.

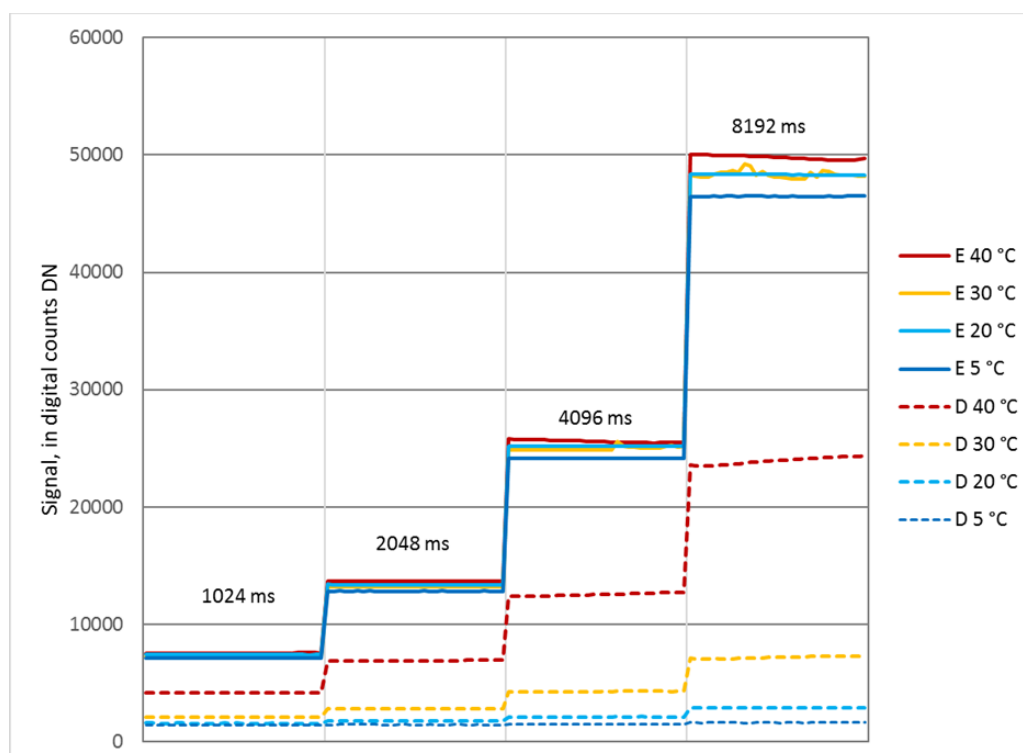


Figure 6-21. Signal and dark signal (dotted line) as a function of integration time and temperature for large integration times.

Dark spectra of SAM\_8114 at pixel 120

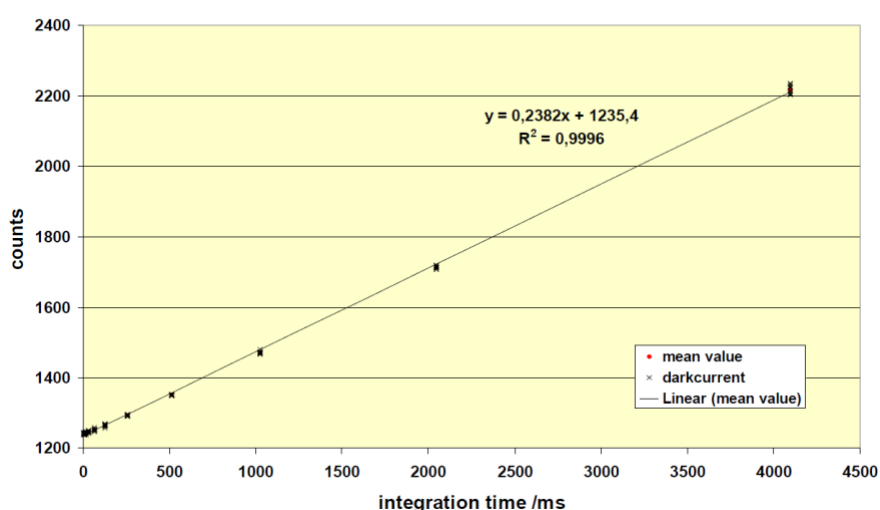


Figure 6-22. Dark signal versus integration time for a single pixel, from the RAMSES user manual Rel. 1.1.

The dark signal of a spectrometer is mainly the sum of two components: (1) the dark current of the detector element, which depends exponentially on the detector's temperature and is proportional to the integration time; (2) the dark current due to additional contributions such as offset of an amplifier circuit. The latter usually depends much less on temperature and integration time, but variability between different instruments can be significant. Due to this, the combined effect in the resulting overall dark signal is complicated and differs significantly from instrument to instrument. The dark signal determined at 8192 ms integration time as a function of temperature for three HyperOCR radiometers is shown in Figure 6-23. Although the temperature dependence is relatively strong, it is difficult to use such a curve for direct evaluation of the sensor's temperature.

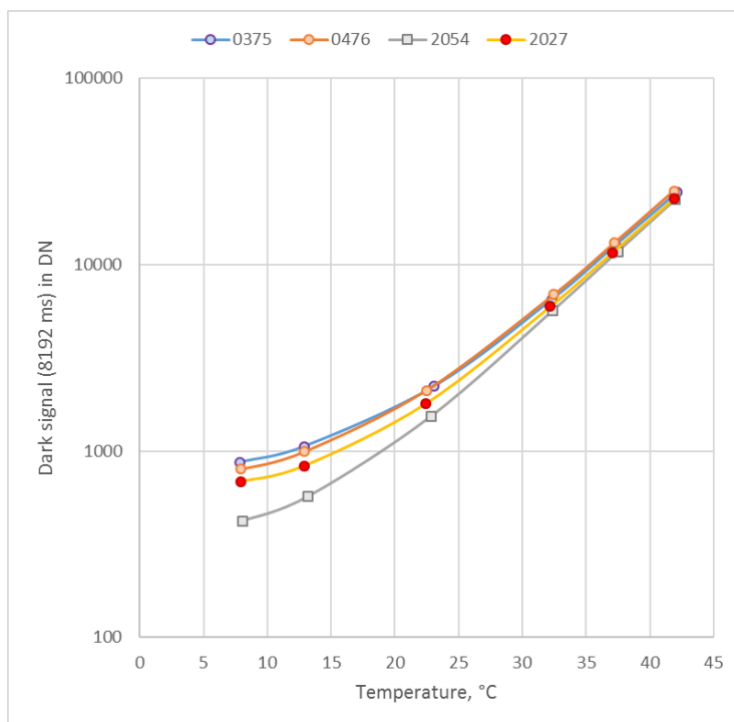


Figure 6-23. Dark signal determined at 8192 ms integration time as a function of temperature for four radiometers.

For HyperOCR sensors, we found an easy method for the effective separation of these two dark signal components. That is subtraction of the dark signal measured with the shortest integration time (4 ms) from the dark signal measured with the longest integration time (8192 ms). The exponential part of the dark signal for four HyperOCR sensors is given in Figure 6-24. Rather similar exponential dependence can also be observed for RAMSES sensors after dark separation by using other approaches. However, lack of shutter is limiting the effective use of the dark signal of the RAMSES during field use. Before using dark signal as temperature reference, characterisation in comparison with SI traceable thermometer in suitable temperature range shall be done.

Inverse functions of the dependence in Figure 6-24 are shown in Figure 6-25, demonstrating the principal range of applicability of the dark signal to determine the temperature of an optical sensor. In order to achieve reasonably small uncertainty, the exponential component of the dark signal should be larger than 100 DN. Thus, with 8 s integration time temperature range from 5 °C to 45 °C can be realised, with 1 s integration time temperature range from 20 °C to 45 °C can be obtained, and with 256 ms integration time temperature range only from 30 °C to 45 °C can be realised. However, for shorter integration times, the reliability of temperature estimates will also be rather modest.

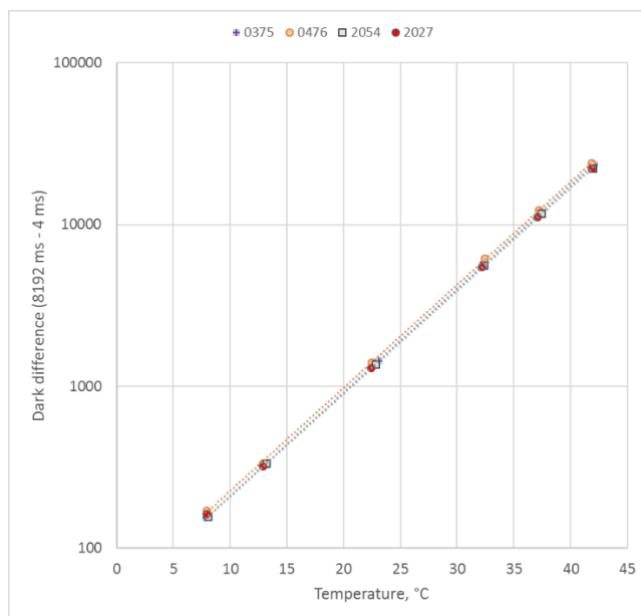


Figure 6-24. Exponential part of the dark signal after subtraction of permanent part, difference  $\Delta D$  of two dark signals,  $D(8\text{ s}) - D(4\text{ ms})$ .

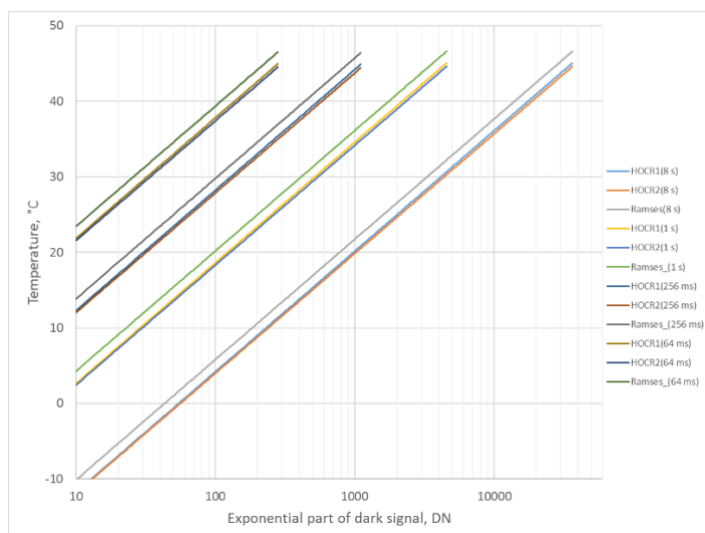
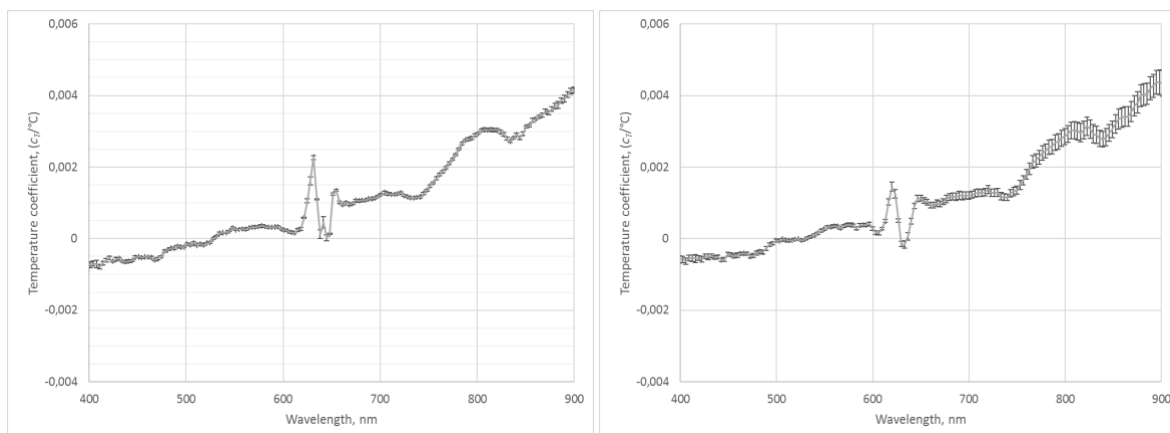


Figure 6-25. Using the exponential part of the dark signal for detection of the sensor's temperature.

## 6.9 Thermal response

Thermal coefficients of two RAMSES and two HyperOCR sensors are presented. For determination of the thermal coefficients, the radiometer was immersed into a cylindrical thermally controlled water tank, equipped with an optical grade fused silica window. The temperature setpoints were selected as +5 °C, +10 °C, +20 °C, +30 °C, +35 °C and +40 °C to cover the expected temperature range evenly as in use. Three integration times have been used at each setpoint to account for the non-linearity effect. At least two scans were performed for each spectrometer, with temperature ramping up and down, respectively. The thermal coefficients for the HyperOCR radiance sensors after correction for non-linearity are given in Figure 6-26, and for HyperOCR irradiance sensor in Figure 6-27. The likely reason for the oscillation observed at ca. 620 nm is the order-sorting filter (OCF) in front of the detector. Order sorting filter is necessary for blocking higher order diffraction of shortwave input signal, however, the first order diffraction must reach the corresponding pixels of the detector array. This implies that the order-sorting filter must cover only part of the detector array. The reflection and refraction properties at the edge

of the filter may be temperature dependent. Thermal coefficients after correction for non-linearity for the RAMSES sensors are given in *Figure 6-28*. The determination of thermal coefficients is described in D-12.



*Figure 6-26. Thermal coefficients of two HyperOCR radiance sensors (0375 and 2054) after correction for non-linearity.*

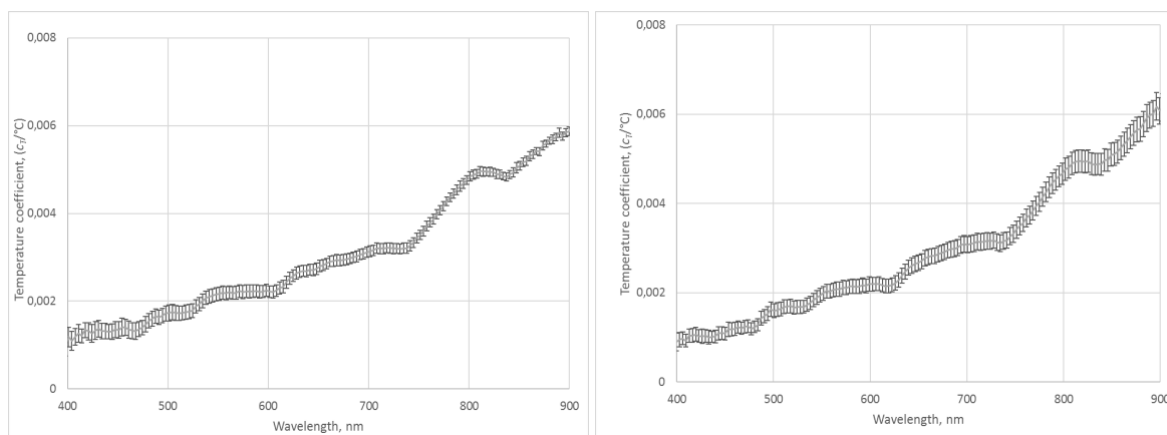


*Figure 6-27. Thermal coefficients of two HyperOCR irradiance sensors (0476 and 2027) after correction for non-linearity.*

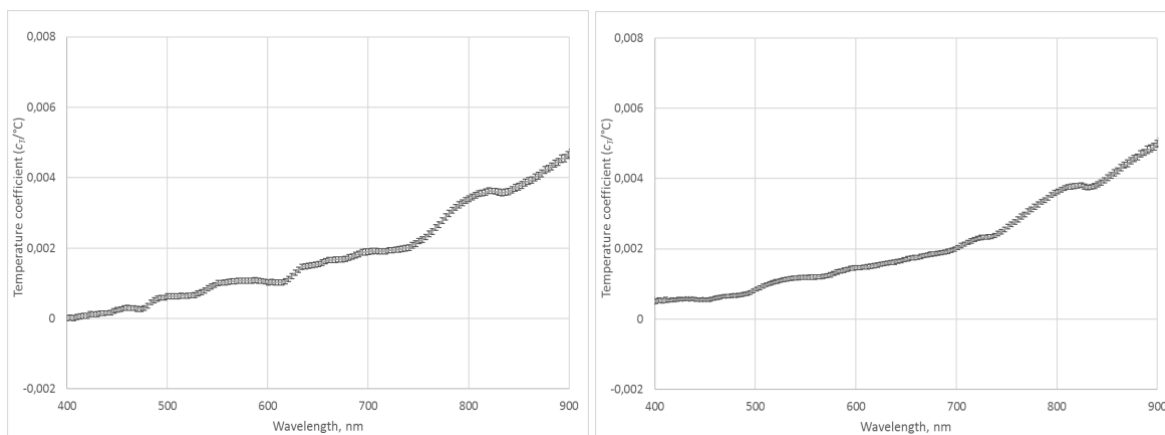


*Figure 6-28. Thermal coefficients of two RAMSES sensors after correction for non-linearity.  
 Left: irradiance (8598); right: radiance (81Bo).*

### 6.9.1 Comparison with previous results

Agreement between average values of thermal coefficients (*Figure 6-29* and *Figure 6-30*) obtained from different sources is satisfactory. Differences between average results of current study and previous data of [16] and [17] in comparison with spread of individual instruments are negligible. However, expanded uncertainty covering the thermal characteristics of [16] does not cover individual characteristics determined during FRM4SOC-2 project. Range of differences between individual thermal coefficients of HyperOCR sensors seems to be somewhat larger than between RAMSES sensors but for safe class-specific description, additional individual characterisation of both radiometer’s models is necessary.

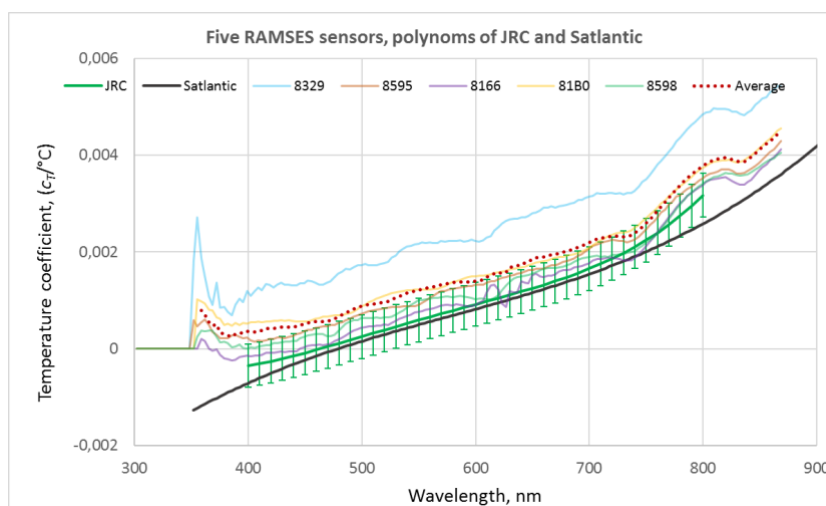


Figure 6-29. Thermal coefficients of five RAMSES sensors: irradiance (8329; 8598); radiance (8595; 8166; 8180). Polynomial of JRC [16] is shown with green line, polynomial of Satlantic’s [17] by black line.

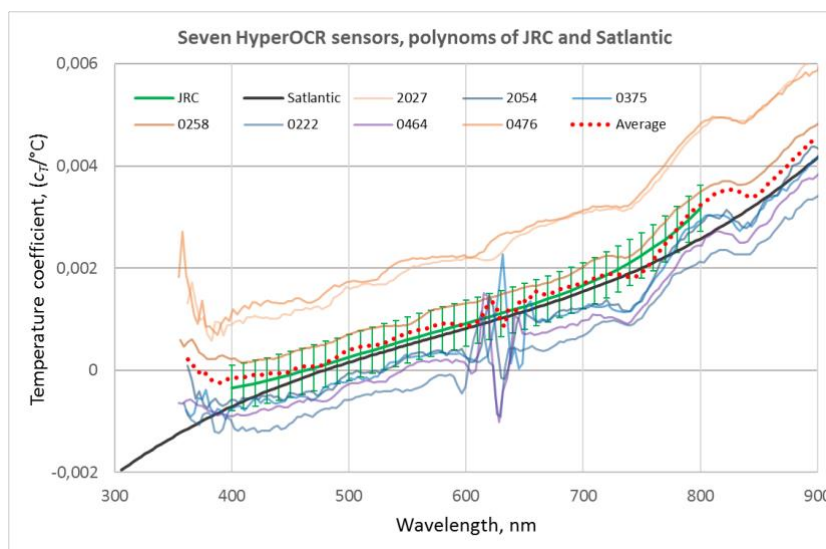


Figure 6-30. Thermal coefficients of seven HyperOCR sensors. Comparison with JRC [16] is shown with green line. Comparison with Satlantic’s data [17] is shown by black line.

Range of differences between individual thermal coefficients of HyperOCR sensors is somewhat larger than between RAMSES sensors. Stronger thermal response of the HyperOCR irradiance sensors besides the contribution of the optical sensor inside the radiometer is likely caused also by the cosine collector made of PTFE. Transmittance of PTFE changes abruptly by 1 - 3 % at around 19 °C due to a phase shift, see for example [18]. Signal jump around 19 °C of HyperOCR irradiance sensors can make its use strongly problematic. Spread of thermal coefficients for 17 RAMSES sensors (9L and 8E) is shown in *Figure 6-31* left and for 8 Hyper-OCR sensors (4L and 4E) is shown in *Figure 6-31* right. Spread of RAMSES irradiance sensors is about 2 times larger than of Hyper-OCR irradiance sensors and spread of RAMSES radiance sensors is about 3 times larger than of Hyper-OCR radiance

sensors. At the same time, the difference between the Hyper-OCR radiance and irradiance sensors is much larger than between the RAMSES radiance and irradiance sensors.

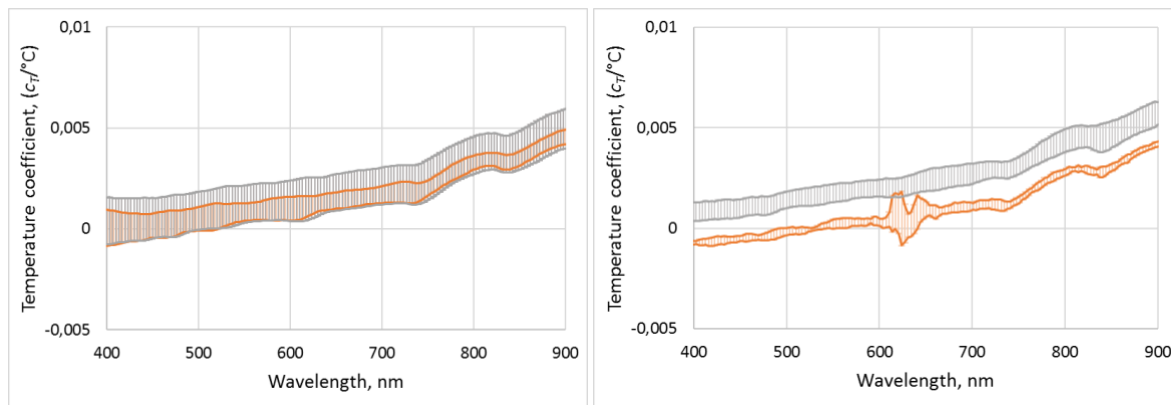


Figure 6-31. Class specific presentation of thermal coefficients. RAMSES left, HyperOCR right. Irradiance sensors are shown with grey, radiance sensors with orange stripes.

Variability of measured spectra of the HyperOCR radiance and irradiance sensors is shown in Figure 6-32 as a function of ambient temperature during thermal responsivity characterisations. Relative thermal effects of HyperOCR radiometers as a function of difference between the working and the calibration temperature is shown in Figure 6-33.

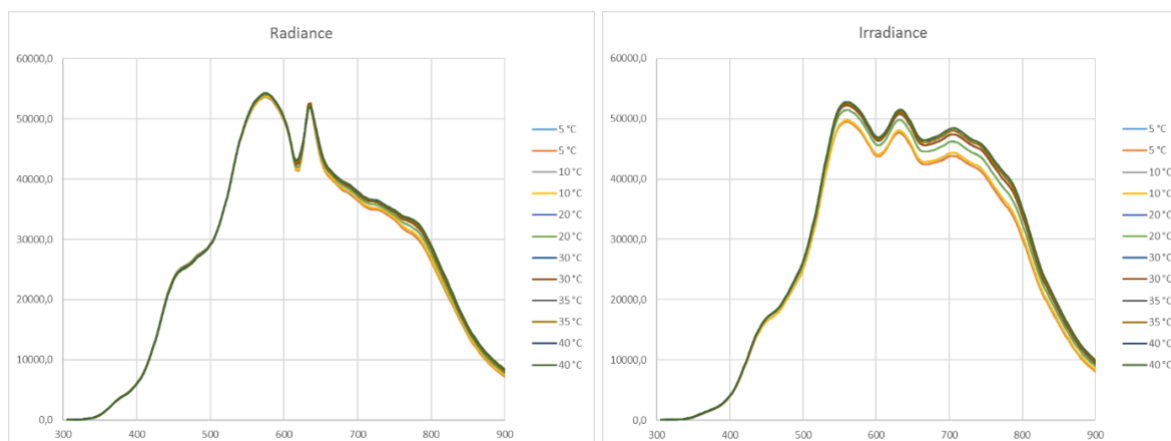


Figure 6-32. Spectra in digital numbers of the HyperOCR radiance and irradiance sensors during thermal characterization as a function of ambient temperature. Radiance sensor left, irradiance sensor right.

In Figure 6-34, relative difference of the thermal variability between the HyperOCR radiance and irradiance sensors as a function of difference between the working and the calibration temperature is shown. The effect in Figure 6-34 – increase of thermal responsivity of irradiance sensor – likely is caused by the thermal sensitivity of the PTFE cosine collector. As a result, in Fig. 4, significant difference between thermal coefficients is evident.



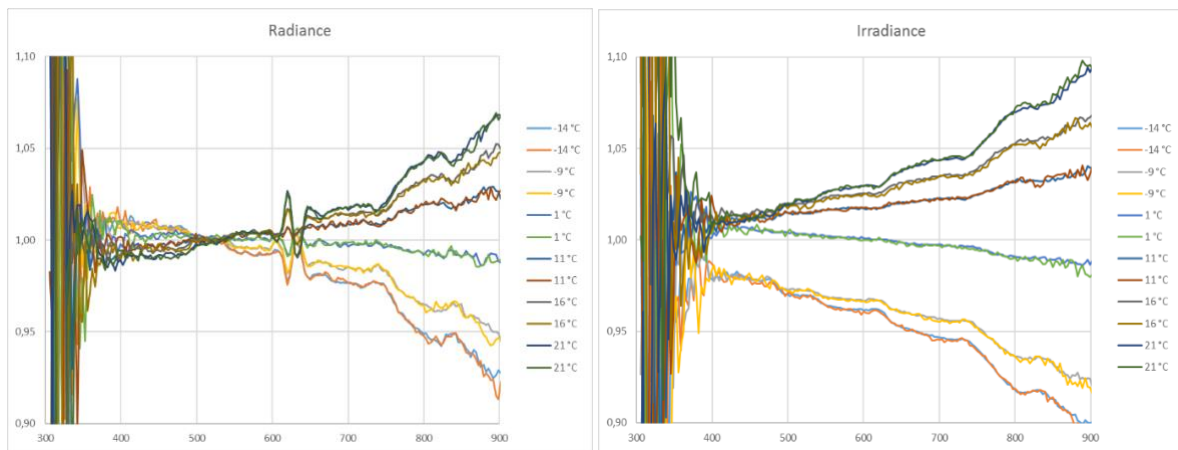


Figure 6-33. Relative thermal variability of HyperOCR radiometers as a function of difference between the working and the calibration temperature. Left: radiance sensor; right: irradiance sensor.

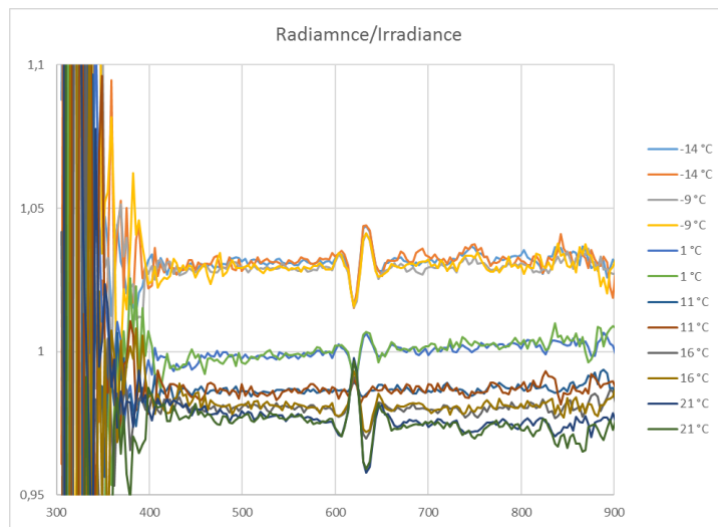


Figure 6-34. Relative difference of the thermal variability between the HyperOCR radiance and irradiance sensors as a function of difference between the working and the calibration temperature.

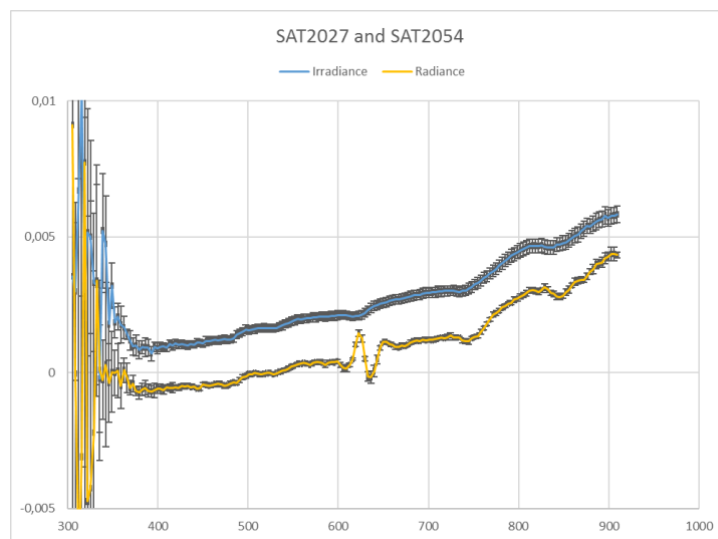


Figure 6-35. Thermal coefficients of HyperOCR sensors (SAT2027-rradiance and SAT2054-radiance).



### 6.9.2 Determination of sensor’s temperature using the dark signal

Due to the rather strong temperature dependence of the dark signal, attempts have been made for TriOS Ramses to use it for the determination of the internal temperature of the radiometer needed for applying temperature correction. For example, a method for correction of temperature effects affecting the miniature spectrometers by using the dark signal is proposed in [19]. However, the attempts made have not been fully successful due to the complicated procedure, limited application range or accuracy.

The main point of the method proposed in this study is in the measurement procedure producing measurement data, which allows effective separation of the two additive dark signal components: (1) the part exponentially depending on the temperature of the optical sensor, and (2) the residual part depending on temperature much more weakly. For that, the dark signal measured with the shortest integration time 4 ms has been subtracted from the measurement with the longest integration time 8192 ms. Using the largest possible difference between integration times is recommended. However, a more effective approach for RAMSES sensors is subtracting finely adjusted constant part from the full dark signal measured with a long integration time. But in the absence of a shutter, this is only possible capping the instrument during operations. Without this procedure, overflows between pixels due to sensor saturation affect the dark measurements [16].

The logarithm function, which is similar for radiometers of the same type, can be used to determine the temperature of the optical sensor of the radiometer. For elimination of small differences, individual calibration constants can be applied in the calculation formula. From exponential component  $\Delta D$  of two dark signals, the temperature of the sensor can be calculated as:

$$t = C_1 \ln\left(\frac{\Delta D}{C_2}\right)$$

$$\Delta D = D(8192 \text{ ms}) - D(4 \text{ ms})$$

$$C_1 = \frac{1}{0.147} \approx 6.8$$

$$C_2 = 50 \pm 3.$$

Constant  $C_1$  is calculated from the mean empirical factor of the exponent, and  $C_2$  is the calibration constant individual for each radiometer.

Table 6-2. Values for  $C_2$  used for calculation.

Device	Constant $C_2$
SAT0375	48
SAT0476	52
SAT2054	48
SAT2027	50

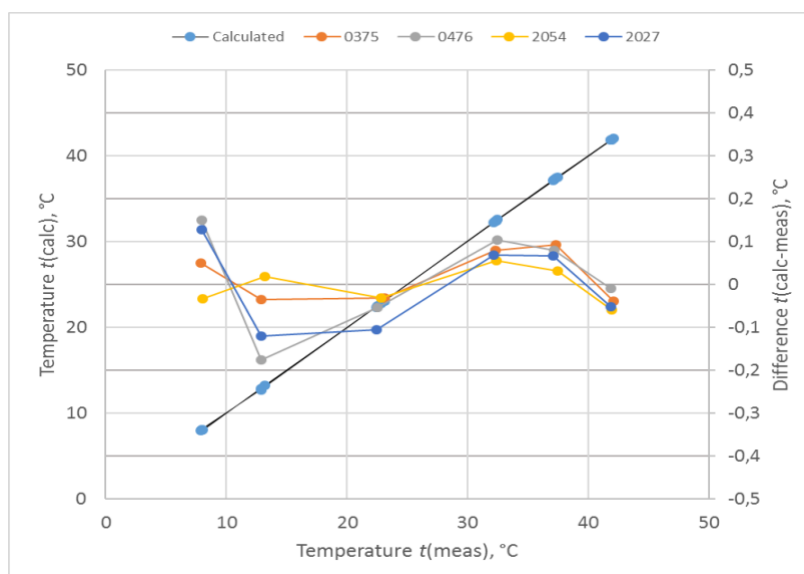


Figure 6-36. Temperature residuals of four radiometers (serial numbers are indicated in the top of the chart).

Results for temperature determination of four HyperOCR radiometers are shown in *Figure 6-36*. Temperature residuals are calculated as the difference between temperatures estimated from the dark signal and measured with the internal sensor.

Differences between the directly measured values and the values calculated from the dark signal remain within  $\pm 0.2$  °C for all four radiometers, and all considered points in the temperature range from 5 °C to 40 °C. The expanded uncertainty of temperature points calculated from the dark signal formula is shown in *Figure 6-37*. The uncertainty increases significantly for lower temperatures due to the separation of the two dark signal components needed for calculation, as the exponential part at lower temperatures will be very small.

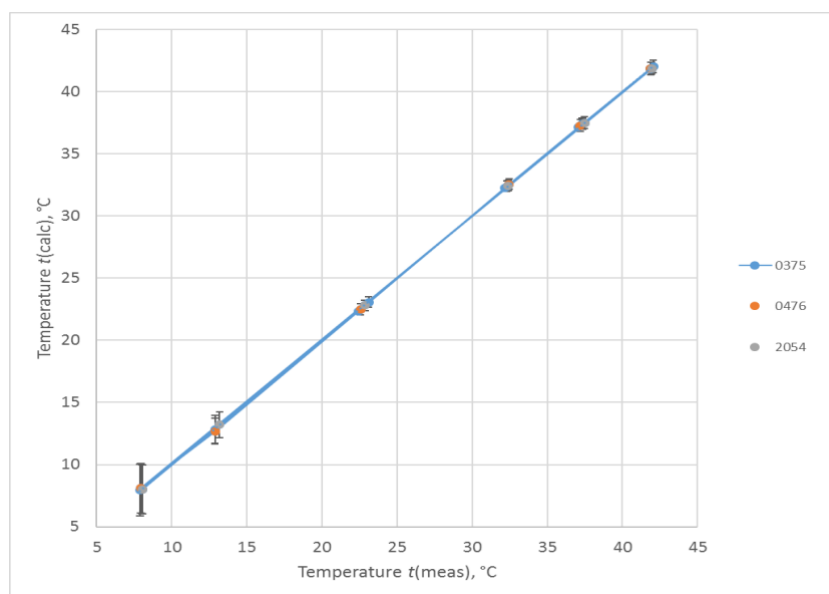


Figure 6-37. Expanded uncertainty of temperature points calculated from dark signal formula.

### 6.9.3 Effects from temperature change

#### Hysteresis of a HyperOCR radiance sensor

In field conditions, the temperature is varying. Special dynamic tests have been performed in a thermostat to evaluate the possible effects from changing temperature on the radiometer measurement signal by sweeping the temperature from 5 °C up to 40 °C and back down to 5 °C. A rather strong hysteresis of the optical signal of the HyperOCR radiance sensor is evident if measured data are presented as a function of the thermostat's temperature (*Figure 6-38*). Here the hysteresis of the optical signal contributes significantly to the measurement uncertainty. The situation is similar to field measurements, where the temperature is obtained with an external temperature sensor. In this case, uncertainty contribution due to hysteresis can be similar or even larger than that due to varying thermal responsivity. Hysteresis becomes significantly smaller if the same data are presented as a function of temperature measured with the internal temperature sensor of the radiometer (*Figure 6-39*). In this case, uncertainty contribution from applying a temperature correction will dominate. Furthermore, if the temperature effect is presented as a function of temperature calculated from the simultaneously measured dark signal of the radiometer, the hysteresis turns out to be rather small and does not contribute significantly to measurement uncertainty (*Figure 6-40*). This effect would be especially important for temperature correction on radiometers without internal temperature sensors, such as TriOS.

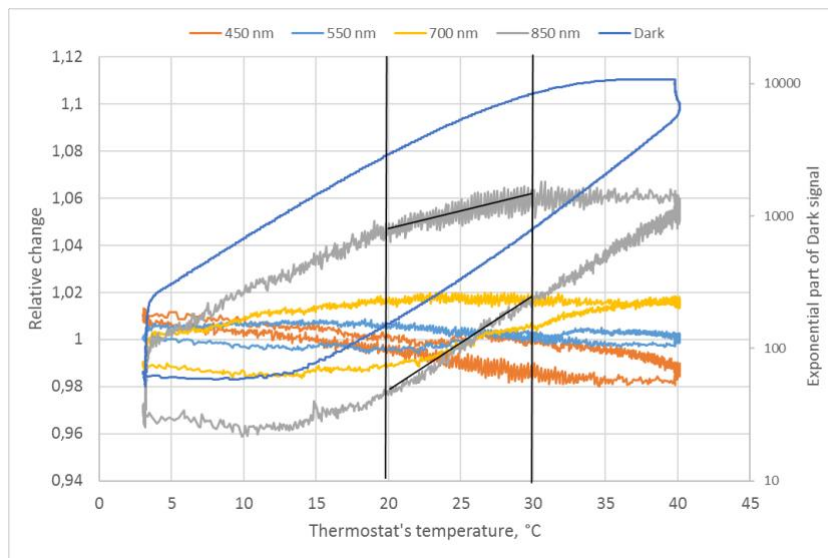


Figure 6-38. Relative change of sensor (0464) signals due to temperature variation as a function of thermostat's temperature.

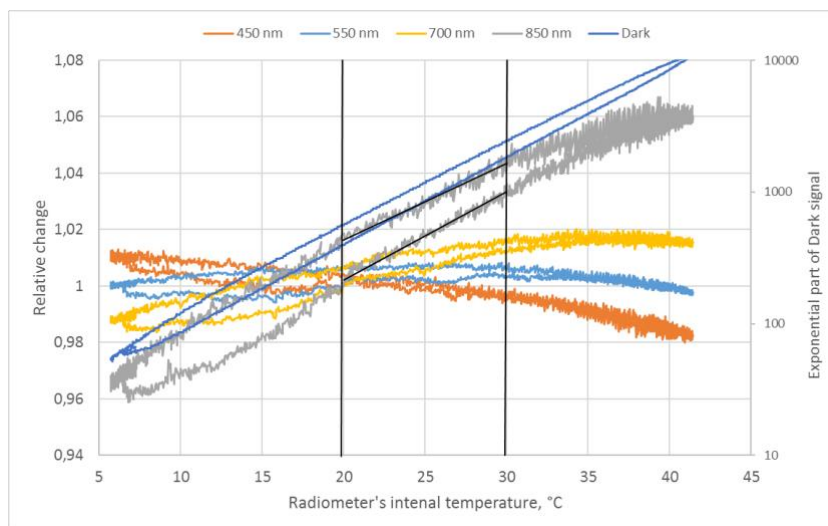


Figure 6-39. Relative change of signals due to temperature variation as a function of temperature measured with the internal temperature sensor of the radiometer (0464).

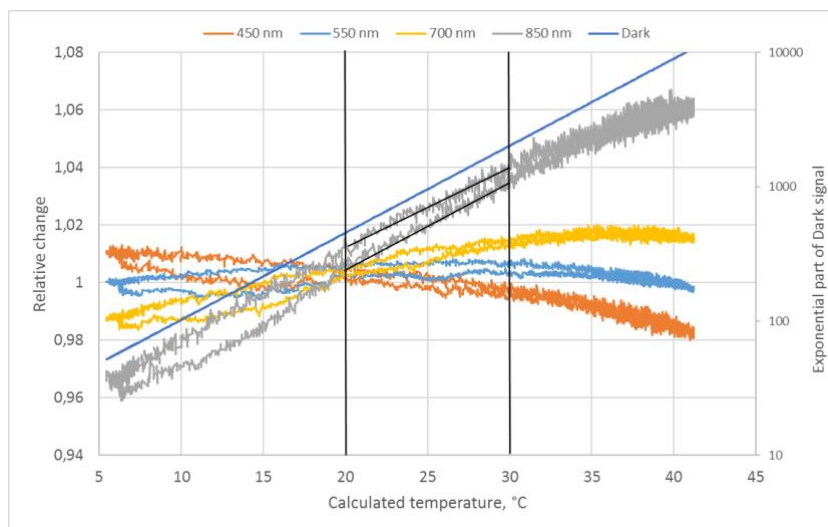


Figure 6-40. Relative change of sensor (0464) signals due to temperature variation as a function of temperature calculated from simultaneously measured dark signal.

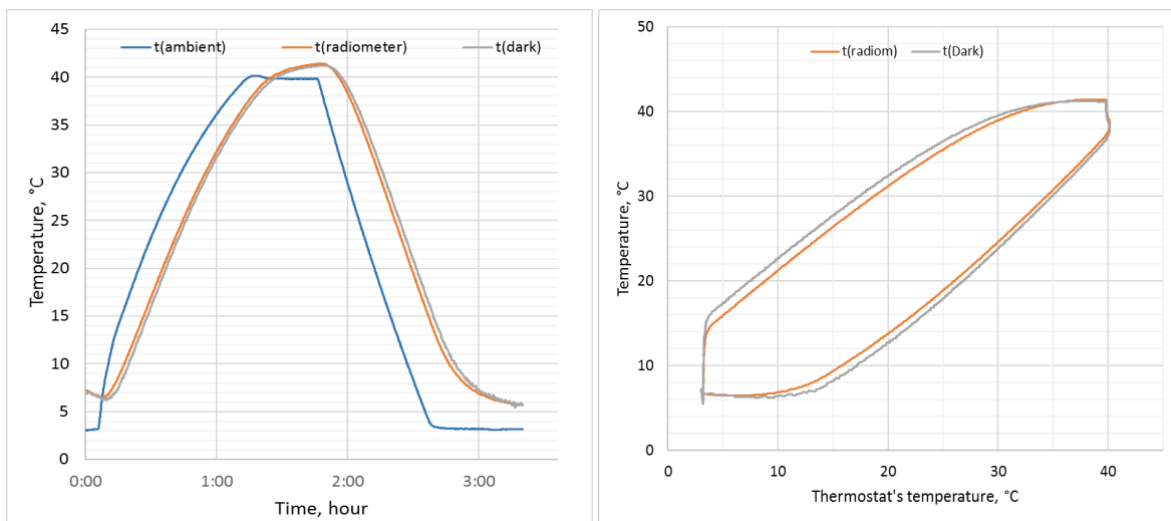


Figure 6-41. Time lags and differences between different temperature sensors. Blue – temperature of the thermostat; orange - internal temperature sensor of the radiometer; grey - temperature calculated from simultaneously measured dark signal.

#### Hysteresis of a HyperOCR irradiance sensor

Strong hysteresis of the optical signal of three HyperOCR irradiance sensors is also evident if measured data are presented as a function of the thermostat's temperature (left side of Figure 6-42, Figure 6-43, and Figure 6-44). In Figure 6-45, relative change of irradiance (0464) as a function of temperature is presented also for temperature calculated from simultaneously measured dark signal. Differently from the radiance sensor, the hysteresis of the optical signal of a HyperOCR irradiance sensors did not decrease substantially if presented as a function of the internal temperature sensor (right side of Figure 6-42, Figure 6-43, Figure 6-44 and Figure 6-45). The likely reason for such a different behaviour is that the thermal response of the irradiance sensor is related to a specific part on the outer surface of the device – the cosine collector made of polytetrafluoroethylene (PTFE) [20] – and not solely the optical sensor inside the radiometer.

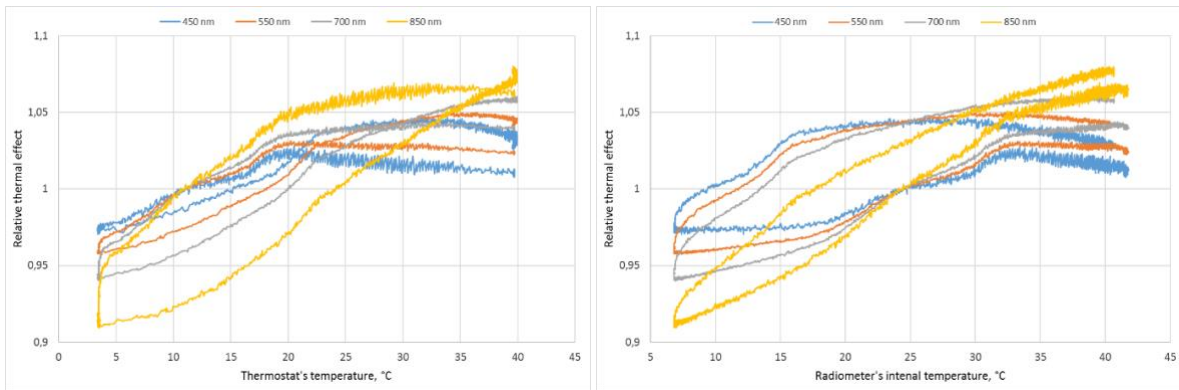


Figure 6-42. Relative change of signals of the irradiance sensor (0496) due to temperature variation as a function of the thermostat's temperature (left) and internal temperature sensor of the radiometer (right).

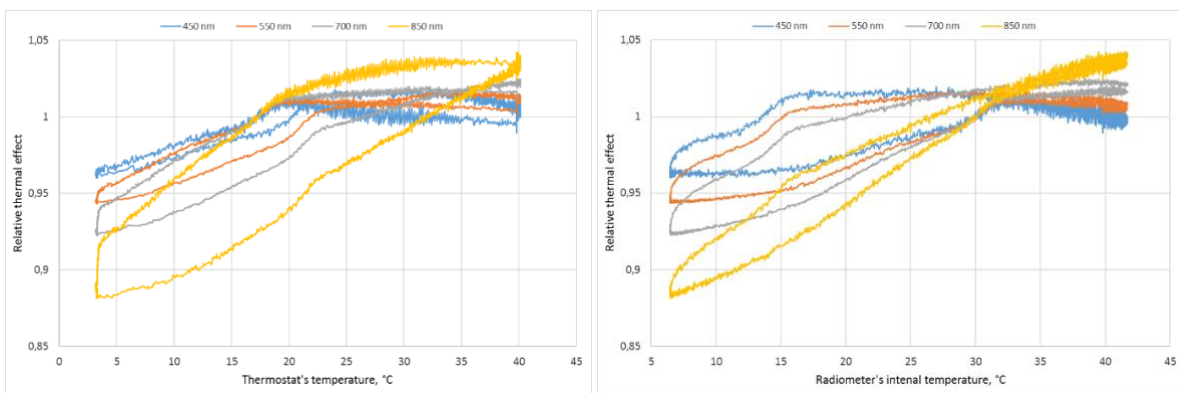


Figure 6-43. Relative change of signals of the irradiance sensor (0464) due to temperature variation as a function of the thermostat's temperature (left) and internal temperature sensor of the radiometer (right).

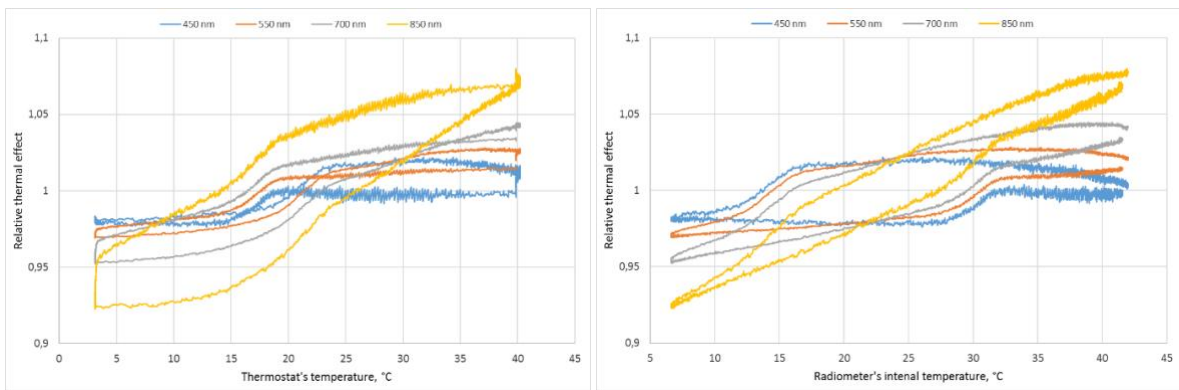


Figure 6-44. Relative change of signals of the irradiance sensor (2027) due to temperature variation as a function of the thermostat's temperature (left) and internal temperature sensor of the radiometer (right).

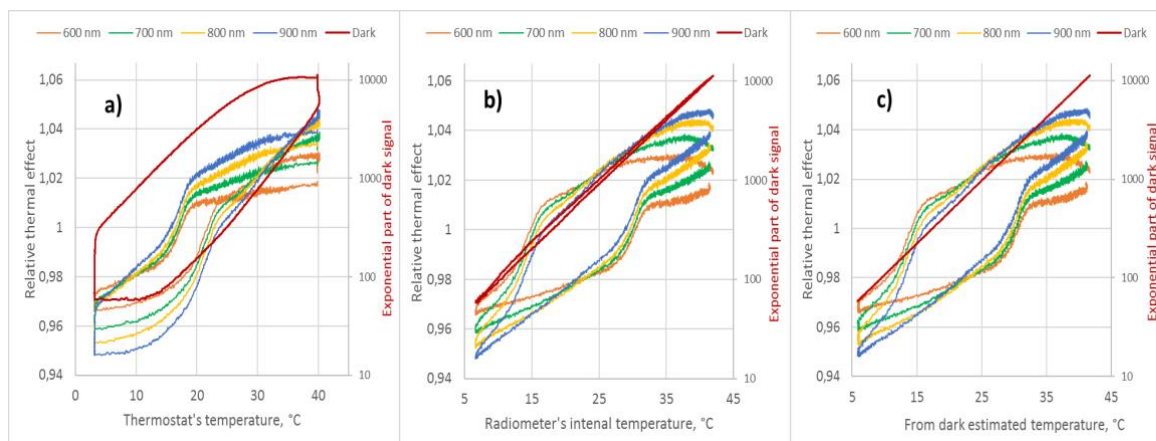


Figure 6-45. Relative change of signals of the irradiance sensor (0464) due to temperature variation:  
 a) as a function of the thermostat's temperature  
 b) as a function of temperature measured with the internal temperature sensor of the radiometer  
 c) as a function of temperature calculated from simultaneously measured dark signal.

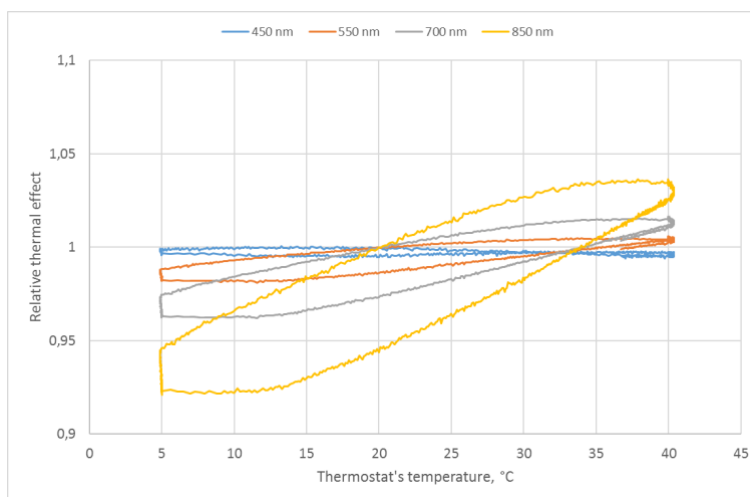


Figure 6-46. Relative change of signals of RAMSES radiance sensor (8595) due to temperature variation as a function of thermostat's temperature.

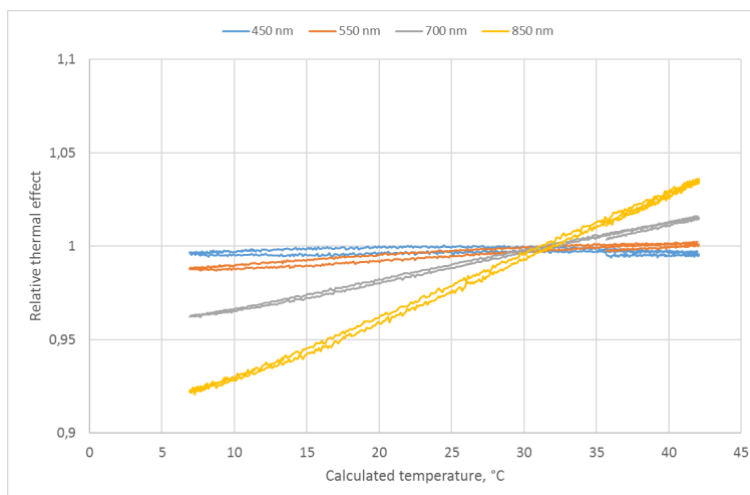


Figure 6-47. Relative change of signals of RAMSES radiance sensor (8595) due to temperature variation as a function of temperature calculated from simultaneously measured dark signal.



Hysteresis of the optical signal of a RAMSES radiance sensor as a function of the thermostat's temperature is shown in *Figure 6-46*. Using the temperature calculated from the dark signal made the hysteresis insignificant (*Figure 6-47*).

Results of *Figure 6-38* to *Figure 6-41* demonstrate the importance of a temperature sensor inside a radiometer used under variable environmental conditions. Somewhat similar or even better results can be obtained by using the exponential part of the dark signal (*Figure 6-47*). During dark measurements used for temperature estimation the instrument has been capped. However, this approach does not substitute the need for an internal temperature sensor, as the reliability of using dark signal for temperature estimation without an internal reference thermometer can not provide SI-traceable temperature results. Still, the method can be applied to radiometers without internal temperature sensors if the dark signal is carefully determined during the characterisation for the thermal responsivity.

### 6.10 Polarisation sensitivity

The polarisation sensitivity of a RAMSES radiometer as a function of wavelength and angle is presented in *Figure 6-48*. The polarisation sensitivity of two HyperOCR radiometers as a function of wavelength and angle is presented in *Figure 6-49* and *Figure 6-50*.

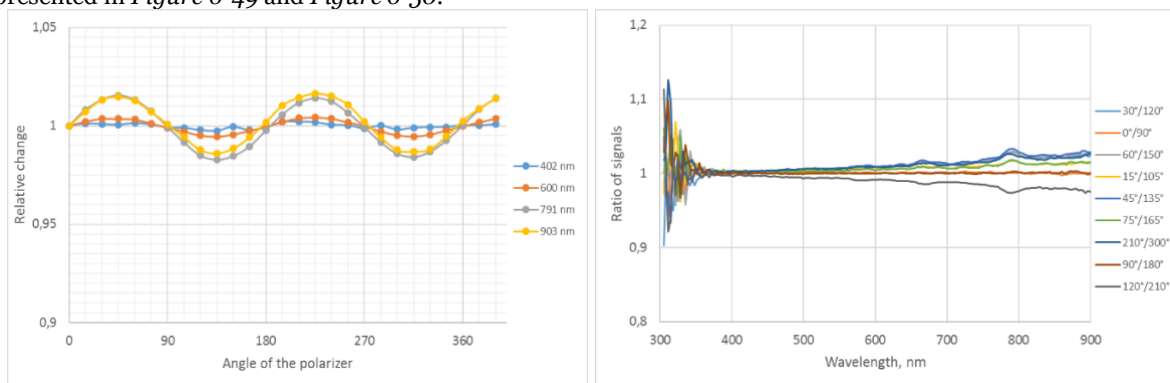


*Figure 6-48. Relative polarisation effect of RAMSES radiance sensor (81Bo) as a function of wavelength and angle.*

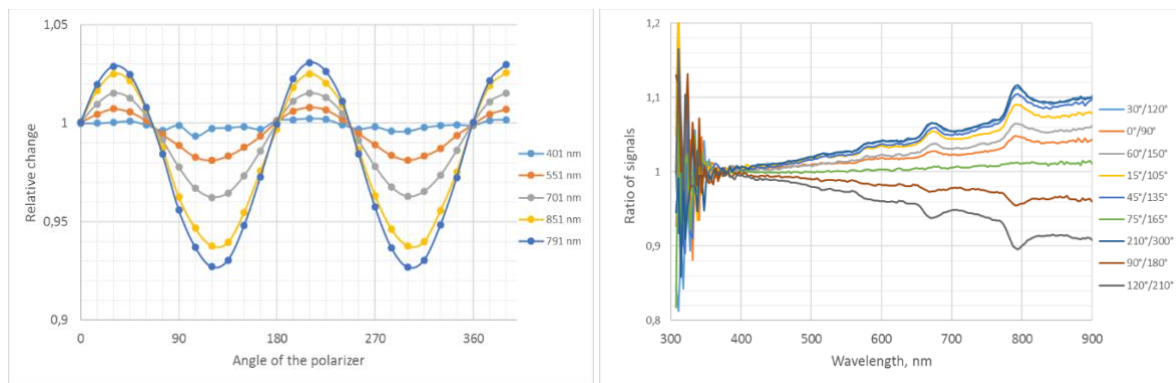


*Figure 6-49. Relative polarisation effect of HyperOCR radiance sensor (0464) as a function of wavelength and angle.*

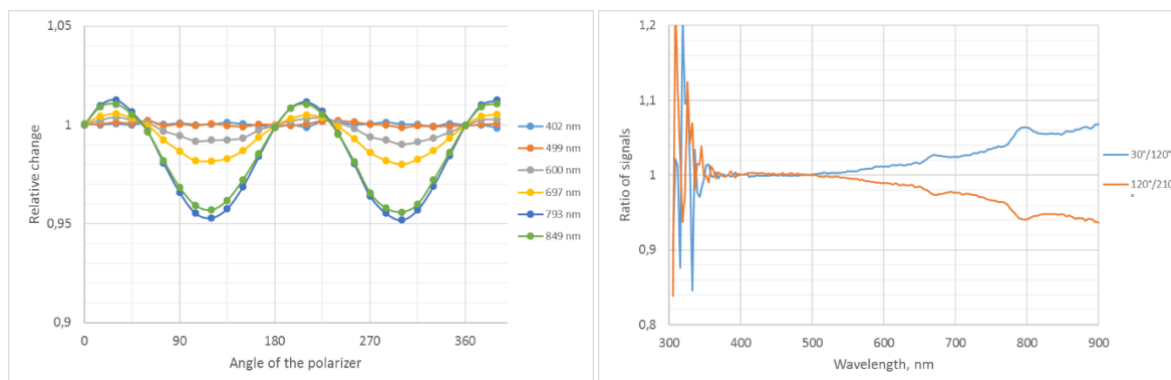


Figure 6-50. Relative polarisation effect of HyperOCR radiance sensor (2054) as a function of wavelength and angle.

### 6.11 Temporal response

Characterisation in process at the time of the writing of the document.

### 6.12 Accuracy of wavelength scale

For all radiometers calibrated and characterised, Kr-lamp spectra have been recorded, maintaining radiometers at different temperatures in the range from 5 °C to 40 °C, see Figure 6-51. Using these Kr-lamp spectra, the accuracy of wavelength scale as a function of temperature was characterised for two RAMSES (81Bo, 8598) and two HyperOCR (2054, 2027) sensors at three different wavelengths and three different temperatures. The results are given in Table 6-4. As the resolution of radiometers is about  $\Delta\lambda$  FWHM  $\approx$  10 nm, then usually more than one Kr line contributes to joint lines recorded by the radiometer. Therefore, two neighbouring Kr lines have been accounted for in all used reference lines listed in Table 6-3. Wavelengths of the Kr lines were obtained from [21]. An example showing the determination of central wavelengths for different temperatures is given in Figure 6-52.

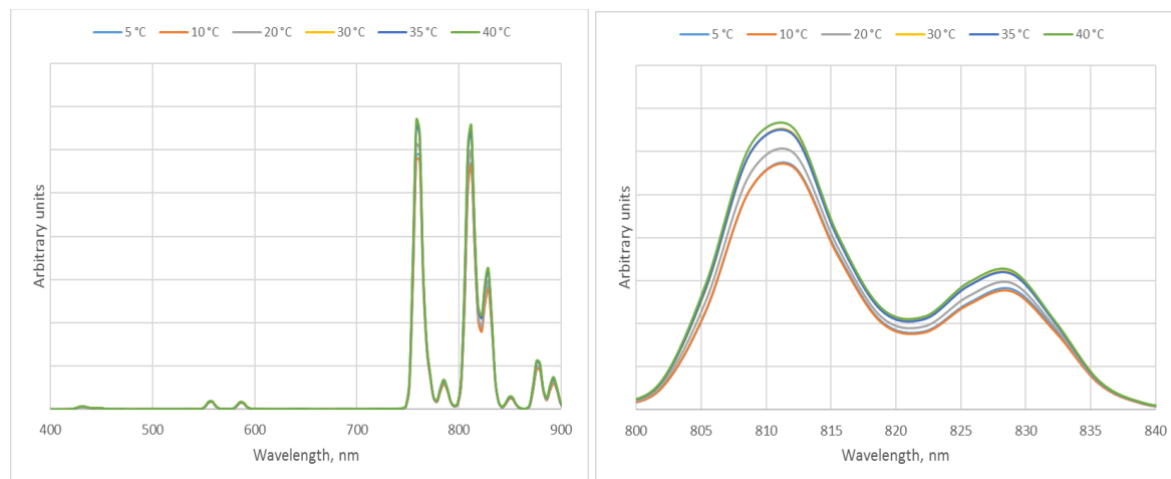


Figure 6-51. Six Kr-lamp spectra as a function of temperature. Right: fraction of spectra - Double line 811 nm/828 nm.



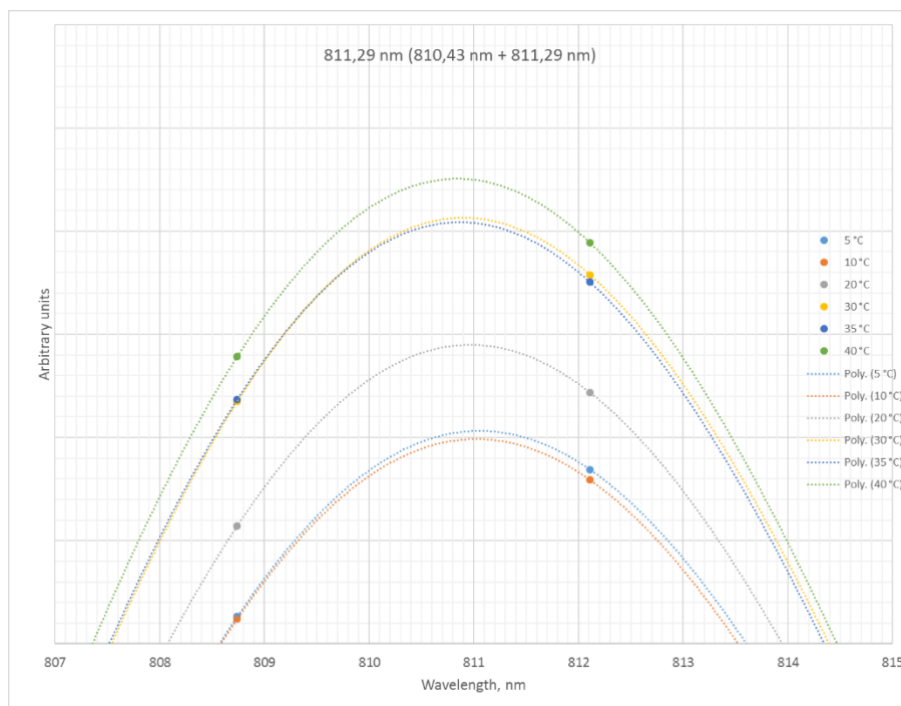


Figure 6-52. Determination of central wavelength of a Kr 811 nm line basing on the approximation polynomials (Poly) calculated for six temperatures from 5 °C to 40 °C .

Table 6-3. Central wavelength of the reference line calculated from two neighbouring Kr lines.

w	$\lambda_1$	$\lambda_2$	w1	w2	w1+w2	$\lambda_{ref}$
Ref1	556.22	557.02	34	163	197	556.88
Ref2	758.74	760.15	1052	3905	4957	759.85
Ref3	810.43	811.29	871	3887	4758	811.13

Table 6-4. Difference of measured wavelengths from Kr-lamp reference values.

Name	Temperature	$\lambda_{meas}$	$\Delta\lambda_1$	$\lambda_{meas}$	$\Delta\lambda_2$	$\lambda_{meas}$	$\Delta\lambda_3$
RAMSES_L(81Bo)	5 °C	557	0.12	759.9	0.05	811.32	0.19
RAMSES_L(81Bo)	20 °C	556.9	0.02	759.95	0.1	811.3	0.17
RAMSES_L(81Bo)	40 °C	556.82	-0.06	759.82	-0.03	811.2	0.07
RAMSES_E(8598)	5 °C	556.75	-0.13	759.77	-0.08	811.05	-0.08
RAMSES_E(8598)	20 °C	556.6	-0.28	759.65	-0.2	811	-0.13
RAMSES_E(8598)	40 °C	556.7	-0.18	759.65	-0.2	810.87	-0.26
HyperOCR_L(2054)	5 °C	556.88	0	759.63	-0.22	810.9	-0.23
HyperOCR_L(2054)	20 °C	556.84	-0.04	759.72	-0.13	810.8	-0.33
HyperOCR_L(2054)	30 °C	556.95	0.07	759.82	-0.03	811.05	-0.08
HyperOCR_L(2054)	40 °C	556.72	-0.16	759.6	-0.25	810.75	-0.38
HyperOCR_E(2027)	5 °C	556.75	-0.13	759.82	-0.03	811.04	-0.09
HyperOCR_E(2027)	20 °C	556.62	-0.26	759.75	-0.1	810.95	-0.18
HyperOCR_E(2027)	40 °C	556.55	-0.33	759.64	-0.21	810.85	-0.28

According to the specification of the MMS-1 module [22], the wavelength accuracy of the module should be better than 0.3 nm, and the temperature drift smaller than 0.01 nm/K. Of the thirty-nine  $\Delta\lambda$  values in Table 6-4 only three values are larger than 0.3 nm. The temperature drift meets the specification for all characterised radiometers. Thus, the wavelength scale of all characterised radiometers is in satisfactory agreement with the reference scale of the Kr lamp.

### 6.13 Signal-to-noise ratio

The signal-to-noise ratio is determined as the ratio of an averaged signal (dark subtracted) to the standard deviation of a single measurement accounting for the scattering of both light and dark signal (recalculated to 1 s integration time).

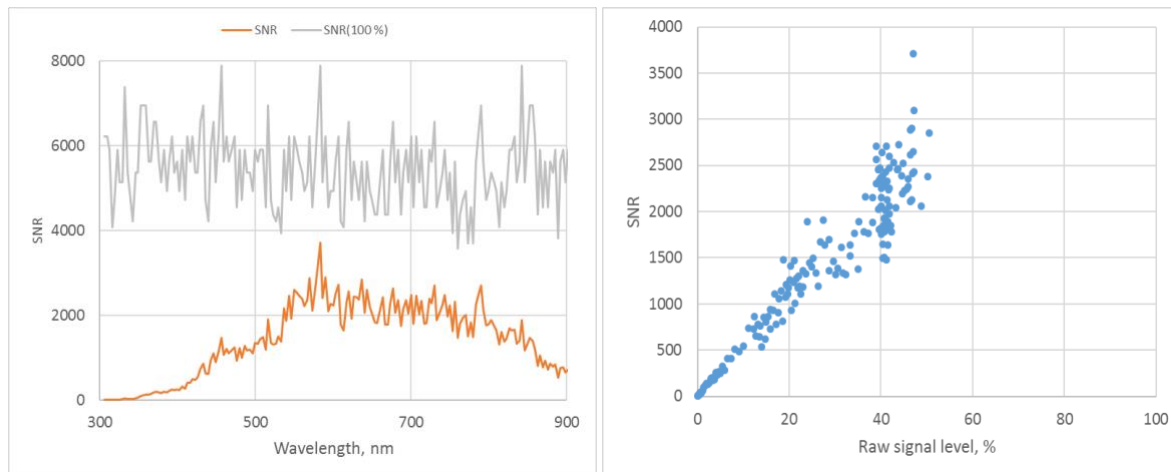


Figure 6-53. The signal-to-noise ratio of a HyperOCR sensor (2054). Spectral dependence (left) and SNR as a function of raw signal (right).

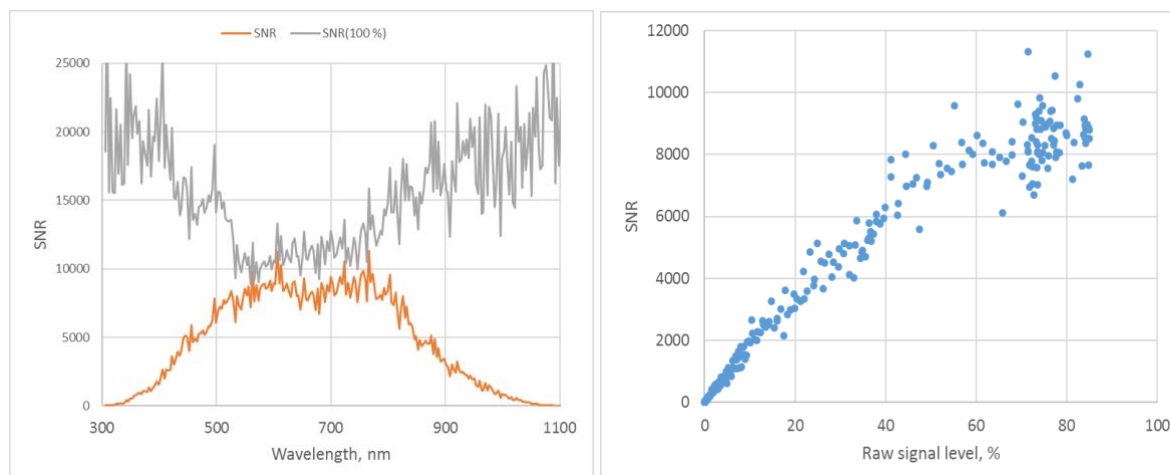


Figure 6-54. The signal-to-noise ratio of a RAMSES sensor (8329). Spectral dependence (left) and SNR as a function of raw signal (right).

The signal-to-noise ratio of a HyperOCR irradiance sensor is shown in Figure 6-53 left. The orange curve is SNR of a lamp spectrum measured during calibration. The grey curve is the same spectrum with SNR values recalculated for the saturation level of the sensor; at this level, maximum values of signal-to-noise ratio for the particular sensor can be expected, see Figure 6-53 right showing the dependence of SNR on the raw signal level, estimated from the same spectrum. Similar data for a RAMSES irradiance sensor is given in Figure 6-54.

Maximum values of signal-to-noise ratios are shown for six RAMSES radiometers (Figure 6-55, left) and for six HyperOCR radiometers (Figure 6-55, right). Presented SN values correspond to maximum values of the sensors, calculated from calibration results and scaled to the full-range value of different sensors. For RAMSES sensors, two groups are seen – irradiance sensors with higher and radiance sensors with lower values. Similarly, but less clearly grouped are HyperOCR sensors. The major difference between RAMSES and HyperOCR is significantly higher (about two times) the level of SN values of RAMSES radiometers.

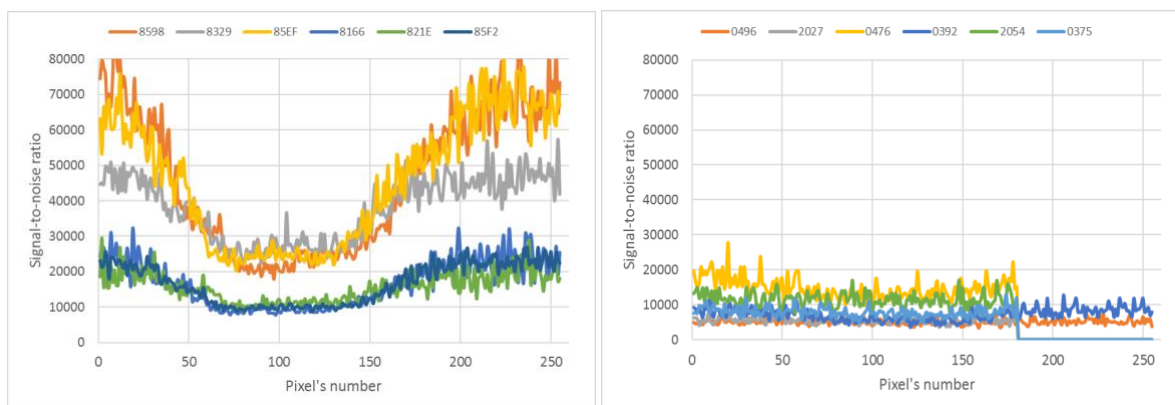


Figure 6-55. Maximum values of signal-to-noise ratios of six RAMSES sensors (left) and six HyperOCR sensors (right). The serial number of the sensor is indicated in top of the chart.

The signal-to-noise ratio at different temperatures is shown in Figure 6-56 for the RAMSES and HyperOCR radiometers. For signals measured with 8192 ms integration time, SN values at higher temperatures are reducing substantially, and smaller than 1000:1 ratios are typical for temperatures above 30 °C.

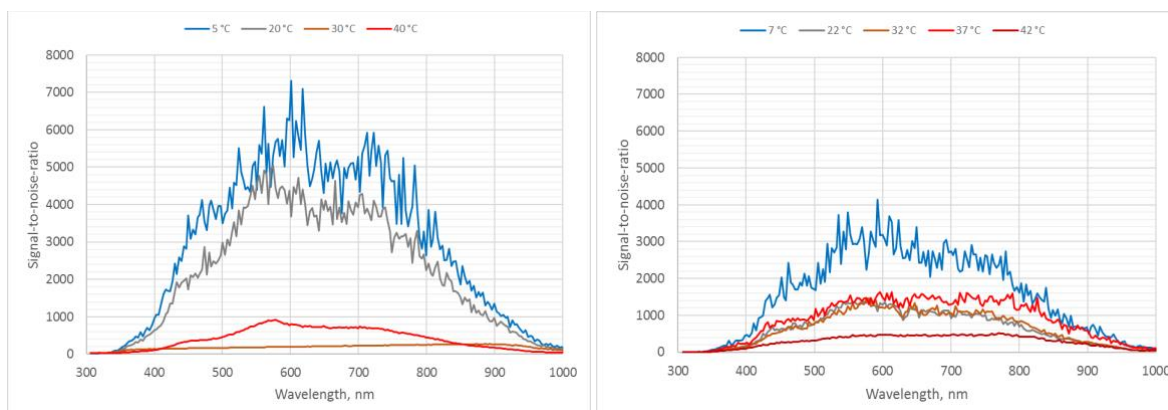


Figure 6-56. Signal-to-noise ratios measured with 8192 ms integration time. RAMSES sensor (81Bo) left, HyperOCR sensor (0375) right.

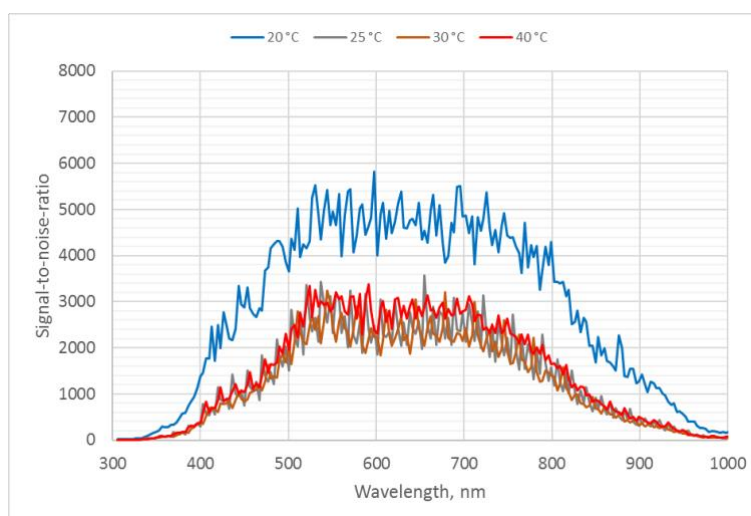


Figure 6-57. Signal-to-noise ratios of a RAMSES sensor (81Bo) measured with 256 ms integration time.

	<p><b>EUMETSAT Contract no. EUM/CO/21/460002539/JIG</b>  <b>Fiducial Reference Measurements for Satellite Ocean</b>  <b>Colour (FRM4SOC Phase-2)</b></p>	<p>Date: 26.04.2023  Page 43 (48)  Ref: FRM4SOC2-TR-D7  Ver: 3.1</p>
--	--	--

Long integration times over 1 s and at a temperature over 20 °C can cause problems like strong autocorrelation in recorded time series, lead to a low signal-to-noise ratio and hinder applying different correction for systematic effects. The main reason for these effects likely is the self-heating of the optical sensor during long integration times. The situation is much better with integration times below 512 ms (*Figure 6-57*). Then, for both types of sensors (RAMSES and HyperOCR) effects of higher temperature on the signal-to-noise ratio are insignificant. In this case, the randomness of time series is quite likely of white noise type, and correction algorithms for systematic effects are performing satisfactorily.

#### **6.14 Pressure effects**

Characterisation in progress at the time of the writing of the document.



	<b>EUMETSAT Contract no. EUM/CO/21/460002539/JIG          Fiducial Reference Measurements for Satellite Ocean          Colour (FRM4SOC Phase-2)</b>	Date: 26.04.2023 Page 44 (48) Ref: FRM4SOC2-TR-D7 Ver: 3.1
--	---	---

## 7 Gaps in characterisation results

Table 7-1. List of parameters not addressed in FRM4SOC phase-1.

<b>Parameter</b>	<b>Plans for characterisation</b>
4. Immersion factor (radiance, irradiance)	To be finalized before the official end of the project
8. Accuracy of integration times	Correct determination of all integration times is possible in cooperation with manufacturers. Can be planned for the project extension.
12. Temporal response	To be finalized before the official end of the project
15. Pressure effects	Postponed. Possible during the project extension.



	<b>EUMETSAT Contract no. EUM/CO/21/460002539/JIG</b> <b>Fiducial Reference Measurements for Satellite Ocean</b> <b>Colour (FRM4SOC Phase-2)</b>	Date: 26.04.2023 Page 45 (48) Ref: FRM4SOC2-TR-D7 Ver: 3.1
--	---	---

## 8 Conclusions

The majority of the characterisations listed in Table 6-1, are carried out and presented for at least four radiometers. The characterisations performed under stable laboratory conditions are in reasonable good agreement with published data. A number of lessons learned during recharacterisation in the frame of FRM4SOC Phase 2 are presented in Table 8-1.

Table 8-1. Lessons learned during recharacterisation in the frame of FRM4SOC Phase 2.

<b>Property/parameter</b>	<b>TriOS RAMSES</b>	<b>HyperOCR</b>
Internal temperature sensor	No	Yes
Mechanical shutter	No	Yes
Black painted pixels	Yes	No
Average power consumption, W	0.85	4
Average internal heating, W	Medium	High
Dependence on integration time	High	Weak
Dependence on shutter	N/A	High
Difference between internal and outside temperature	About 2 °C	(3...4) °C
Thermal characteristics of L and E sensors	Close	Different
Signal hysteresis in varying conditions	Strong, ±3 %	Strong, ±3 %
Hysteresis of irradiance sensors is caused by	Internal parts	Internal and diffuser
Materials used for cosine collector	Stable	Unstable at temperature of about (19...20) °C due to PTFE phase jump
Signal-to-Noise ratio	2×	1×
Efficiency of characterisation due to SNR	Satisfactory	Weak
Dark signal level at 40 °C (longest integration time)	About half of DR	About half of DR
Reliability during longer tests at 40 °C	90 %	100 %
Instability during a year	About 1 %	About 1 %
Maximum non-linearity error	About (2...3) %	About (2...3) %
Dependence on temperature of NL coefficients	Weak	Significant
Stray light matrix, noise level	Satisfactory	Higher noise
Angle characteristics depending on the azimuth	Often evident	Seldom
Specification for cosine collector	6-10 %	3 % at 0–60°
Irradiance, conformance to specification	Yes	Yes
Signal oscillation due to order-sorting filter	Not detected	Often present for radiance sensors
Polarisation sensitivity	1×	3×
Integration time accuracy	Conforming, range (4...8192) ms	Conforming, range (8...8192) ms
Nonconforming integration times Seabird's OCR Radiance, Irradiance	Often 4.05 ms instead of stated 4 ms	Often 5 ms instead of stated 4 ms
<b>Software, similarity of operation modes</b>		
Convenient software for field measurements	Not provided by the manufacturer	
Dark signal handling in whole data handling chain	Fundamentally different	
Integration time selection	Possible	Time-consuming
Communication speed	Slow	Medium
Ramses G2 communication speed	Extremely slow	N/A
Ramses G2	Serial number not hard coded into the instrument	N/A
Ramses G2	Same plug with Hyper OCR, but different wiring	N/A
<b>Possible issued detected</b>		
Characterisation at 40 °C	Risk of failure of irradiance sensors	Failures not detected;
Nonconforming integration times at 4 ms	Not detected	Often 5 ms instead of stated 4 ms
Responsivity decay at shorter wavelengths	In the range (300...400) nm	Not detected/not available
Pixel 31/32 error with IP module	Rare software bug in the communication between the inclination module and the spectrometer.	N/A
<b>Servicing/repair by manufacturer</b>	Not easily accessible	



	<p align="center"><b>EUMETSAT Contract no. EUM/CO/21/460002539/JIG Fiducial Reference Measurements for Satellite Ocean Colour (FRM4SOC Phase-2)</b></p>	<p>Date: 26.04.2023 Page 46 (48) Ref: FRM4SOC2-TR-D7 Ver: 3.1</p>
--	---	---

Some key points from the characterisation measurements in FRM4SOC phase-2.

- Angle characteristics of TriOS RAMSES irradiance sensors are often strongly non-symmetrical and thus, depend on the azimuth angle used for measurements. This circumstance also makes the further use of characterisation results much more difficult: azimuth angle must be specified during characterisation and during later use.
- Following [AD-4], the integration time characterisation has been performed together with non-linearity characterisation by looking at a constant source and measuring this source at different integration times. The method used for non-linearity determination gives valid results only if the correctness of realised integration times is evident. From several measurements (with more than 40 sensors), non-conformance of actual integration time in relation to the set value has been detected in most HyperOCR sensors for the shortest integration time of 4 ms. In the case of the RAMSES instruments, for the shortest integration time the actual integration time is around 4.05 ms instead of 4 ms. The non-linearity of most sensors is slightly temperature dependent, but for the HyperOCR irradiance sensors, the effect is more significant - achieving about 10 % - at higher temperatures.
- Determination of the sensor's temperature and effects caused by temperature change during field measurements by using the dark signal are innovative in many ways. Results in *Figure 6-38* to *Figure 6-41* demonstrate clearly the importance of an internal temperature sensor of a radiometer used under variable environmental conditions. Correcting for temperature effects is inefficient without an internal temperature sensor due to the large uncertainty of the determined temperature difference under calibration and use in-field. Large hysteresis of the optical signal determined during the increasing and decreasing temperature cycle also implies a significant increase in uncertainty.

Using the exponential part of the dark signal to calculate the temperature of an optical sensor will reduce the hysteresis of the optical signal substantially in comparison to using external temperature. However, dark signal can not substitute the internal temperature sensor, as without internal reference thermometer SI-traceability of temperature estimates obtained by this method is not granted. However, this effect can still be applied to radiometers without internal temperature sensors when the dark signal is carefully determined during the characterisation of the thermal responsivity. If an internal temperature sensor was available, then the differences between the directly measured temperature values and the values calculated from the dark signal remained within  $\pm 0.2$  °C for four characterised radiometers in the temperature range from 5 °C to 40 °C. The expanded uncertainty of the temperature points calculated from the dark signal formula is about 0.5 °C from 15 °C to 40 °C and increased for lower temperatures up to 2 °C. The increase of the uncertainty at lower temperatures is caused by the separation of the dark signal components needed for temperature calculation, as the exponential part of dark signal usually is very small at lower temperatures.

- Change of the radiometric response due to the self-heating in stable lab conditions can distort the calibration and characterisation results. For example, small deviations in spectra due to polarization and/or angular effects can be of the same magnitude as the responsivity change of the radiometer. The radiometer's response will drift with the varying internal temperature due to the mode of data acquisition process. Temperature can rise, but it can also drop if the previous state of the sensor caused more self-heating. Due to internal self-heating, achieving good reproducibility of the characterisation results may be rather difficult. Because of this, regular recording of specified reference signal between routine characterization steps is strongly advisable.
- An interesting effect was revealed during characterisation, regarding the material used for the cosine collector of the HyperOCR irradiance sensor. The angular response of the HyperOCR sensors measured under stable conditions is generally much better than the same characteristics of the RAMSES sensors. However, the temperature dependence of HyperOCR irradiance sensors can make its use strongly problematic. The thermal instability [20] of the cosine collector will hinder its characterisation with small uncertainty and can substantially contribute to the uncertainty of results obtained during field measurements.

The characterisation in stable conditions is essential but insufficient for successful uncertainty evaluation. Therefore, characterisation procedures for determining the sensors' performance in varying conditions need further study and elaboration.





	<p align="center"><b>EUMETSAT Contract no. EUM/CO/21/460002539/JIG</b>  <b>Fiducial Reference Measurements for Satellite Ocean</b>  <b>Colour (FRM4SOC Phase-2)</b></p>	<p>Date: 26.04.2023  Page 47 (48)  Ref: FRM4SOC2-TR-D7  Ver: 3.1</p>
--	---	--

## 9 References

- [1] “JCGM 200:2008: International Vocabulary of Metrology - Basic and General Concepts and Associated Terms (VIM).” BIPM, Aug. 2011.
- [2] J. L. Mueller *et al.*, “Ocean Optics Protocols For Satellite Ocean Color Sensor Validation, Revision 4. Volume III: Radiometric Measurements and Data Analysis Protocols.”, 2003, doi: <http://dx.doi.org/10.25607/OBP-62>.
- [3] S. B. Hooker *et al.*, “The Seventh SeaWiFS Intercalibration Round-Robin Experiment (SIRREX-7), TM-2003-206892, vol. 17, NASA Goddard Space Flight Center, Greenbelt,” Feb. 2002, Accessed: Feb. 08, 2017. [Online]. Available: <http://ntrs.nasa.gov/search.jsp?R=20020045342>
- [4] L. Ylianttila, R. Visuri, L. Huurto, and K. Jokela, “Evaluation of a Single-monochromator Diode Array Spectroradiometer for Sunbed UV-radiation Measurements¶,” *Photochem. Photobiol.*, vol. 81, no. 2, pp. 333–341, 2005, doi: 10.1111/j.1751-1097.2005.tb00192.x.
- [5] G. Seckmeyer, “Instruments to Measure Solar Ultraviolet Radiation Part 4: Array Spectroradiometers (lead author: G. Seckmeyer) (WMO/TD No. 1538). 44 pp. November 2010.” WMO, 2010.
- [6] C. Johnson, H. Yoon, J. P. Rice, and A. C. Parr, “Chapter 1.2 - Principles of Optical Radiometry and Measurement Uncertainty,” in *Experimental Methods in the Physical Sciences*, vol. 47, G. Zibordi, C. J. Donlon, and A. C. Parr, Eds. Academic Press, 2014, pp. 13–67. doi: 10.1016/B978-0-12-417011-7.00003-9.
- [7] S. G. R. Salim, E. R. Woolliams, and N. P. Fox, “Calibration of a Photodiode Array Spectrometer Against the Copper Point,” *Int. J. Thermophys.*, vol. 35, no. 3–4, pp. 504–515, May 2014, doi: 10.1007/s10765-014-1609-1.
- [8] “IOCCG Protocol Series (2019). Protocols for Satellite Ocean Colour Data Validation: In Situ Optical Radiometry. Zibordi, G., Voss, K. J., Johnson, B. C. and Mueller, J. L. IOCCG Ocean Optics and Biogeochemistry Protocols for Satellite Ocean Colour Sensor Validation, Volume 3.0,” IOCCG, Dartmouth, NS, Canada, 2019. doi: <http://dx.doi.org/10.25607/OBP-691>.
- [9] V. Vabson *et al.*, “Laboratory Intercomparison of Radiometers Used for Satellite Validation in the 400–900 nm Range,” *Remote Sens.*, vol. 11, no. 9, p. 1101, Jan. 2019, doi: 10.3390/rs11091101.
- [10] V. Vabson *et al.*, “Field Intercomparison of Radiometers Used for Satellite Validation in the 400–900 nm Range,” *Remote Sens.*, vol. 11, no. 9, p. 1129, Jan. 2019, doi: 10.3390/rs11091129.
- [11] J. Kuusk, I. Ansko, V. Vabson, M. Ligi, and R. Vendt, “Protocols and Procedures to Verify the Performance of Fiducial Reference Measurement (FRM) Field Ocean Colour Radiometers (OCR) used for Satellite Validation,” Tartu Observatory, Tõravere, Technical Report TR-5, Oct. 2017.
- [12] CIE TC 2-78, “CIE TN 010:2019 Determination of the Optical Beam Axis, Centre Beam Intensity, and Beam Angle of Directional Light Sources,” International Commission on Illumination (CIE). doi: 10.25039/TN.010.2019.
- [13] M. Talone and G. Zibordi, “Non-linear response of a class of hyper-spectral radiometers,” *Metrologia*, vol. 55, no. 5, pp. 747–758, Sep. 2018, doi: 10.1088/1681-7575/aadd7f.
- [14] M. Talone, G. Zibordi, and A. Bia\lek, “Reduction of non-linearity effects for a class of hyper-spectral radiometers,” *Metrologia*, vol. 57, no. 2, p. 025008, Mar. 2020, doi: 10.1088/1681-7575/ab6277.
- [15] “TriOS Ramses hyperspectral radiometers. User manual.” TriOS GmbH, 2004.
- [16] G. Zibordi, M. Talone, and L. Jankowski, “Response to Temperature of a Class of In Situ Hyperspectral Radiometers,” *J. Atmospheric Ocean. Technol.*, vol. 34, no. 8, pp. 1795–1805, Aug. 2017, doi: 10.1175/JTECH-D-17-0048.1.
- [17] “Satlantic Instrument File Standard Satlantic’s Data Format Standard for calibration and Telemetry Definition Files SAT-DN-00134, Ver 6.1, 02/04/2010.” Satlantic, 2010.
- [18] L. Ylianttila and J. Schreder, “Temperature effects of PTFE diffusers,” *Opt. Mater.*, vol. 27, no. 12, pp. 1811–1814, Dec. 2005, doi: 10.1016/j.optmat.2004.11.008.
- [19] J. Kuusk, “Dark Signal Temperature Dependence Correction Method for Miniature Spectrometer Modules,” *J. Sens.*, vol. 608157, pp. 1–9, 2011, doi: 10.1155/2011/608157.
- [20] C. P. Ball *et al.*, “Effect of polytetrafluoroethylene (PTFE) phase transition at 19 °C on the use of Spectralon as a reference standard for reflectance,” *Appl. Opt.*, vol. 52, no. 20, pp. 4806–4812, Jul. 2013, doi: 10.1364/AO.52.004806.
- [21] T. Jacksier and R. M. Barnes, “Atomic Emission Spectra of Xenon, Krypton, and Neon: Spectra from 200 to 900 nm by Sealed Inductively Coupled Plasma/Atomic Emission Spectroscopy,” *Appl. Spectrosc.*, vol. 48, no. 1, pp. 65–71, Jan. 1994, doi: 10.1366/0003702944027543.
- [22] “ZEISS Spectrometer Modules Compendium of products, electronic components and software solutions.”

## 10 Acknowledgement

This work has made use of the laboratory facilities of Tartu Observatory, University of Tartu also funded by the Estonian Research Council project TT8 and the Estonian State Shared Service Center project KosEST.



PROGRAMME OF  
THE EUROPEAN UNION

